Nonprecipitating Shallow Cumulus Convection Is Intrinsically Unstable to Length Scale Growth

Janssens, Martin; Vilà-Guerau De Arellano, Jordi; Van Heerwaarden, Chiel C.; De Roode, Stephan R.; Siebesma, A. Pier; Glassmeier, Franziska

DOI
10.1175/JAS-D-22-0111.1

Publication date
2023

Document Version
Final published version

Published in
Journal of the Atmospheric Sciences

Citation (APA)
Janssens, M., Vilà-Guerau De Arellano, J., Van Heerwaarden, C. C., De Roode, S. R., Siebesma, A. P., & Glassmeier, F. (2023). Nonprecipitating Shallow Cumulus Convection Is Intrinsically Unstable to Length Scale Growth. *Journal of the Atmospheric Sciences*, *80*(3), 849-870. https://doi.org/10.1175/JAS-D-22-0111.1

Nonprecipitating Shallow Cumulus Convection Is Intrinsically Unstable to Length Scale Growth

MARTIN JANSSENS,[a,b] JORDI VILÀ-GUERAU DE ARELLANO,[a] CHIEL C. VAN HEERWAARDEN,[a] STEPHAN R. DE ROODE,[b] A. PIER SIEBESMA,[b,c] AND FRANZISKA GLASSMEIER[b]

[a] *Meteorology and Air Quality Department, Wageningen University and Research, Wageningen, Netherlands*
[b] *Geoscience and Remote Sensing Department, Delft University of Technology, Delft, Netherlands*
[c] *Royal Netherlands Meteorological Institute, de Bilt, Netherlands*

(Manuscript received 13 May 2022, in final form 21 November 2022)

ABSTRACT: Condensation in cumulus clouds plays a key role in structuring the mean, nonprecipitating trade wind boundary layer. Here, we summarize how this role also explains the spontaneous growth of mesoscale [$>O(10)$ km] fluctuations in clouds and moisture around the mean state in a minimal-physics, large-eddy simulation of the undisturbed period during BOMEX on a large [$O(100)$ km] domain. Small, spatial anomalies in condensation in cumulus clouds, which form on top of small moisture fluctuations, power circulations that transport moisture, but not heat, from dry to moist regions, and thus reinforce the condensation anomaly. We frame this positive feedback as a linear instability in mesoscale moisture fluctuations, whose time scale depends only on (i) a vertical velocity scale and (ii) the mean environment's vertical structure. In our minimal-physics setting, we show both ingredients are provided by the shallow cumulus convection itself: it is intrinsically unstable to length scale growth. The upshot is that energy released by clouds at kilometer scales may play a more profound and direct role in shaping the mesoscale trade wind environment than is generally appreciated, motivating further research into the mechanism's relevance.

KEYWORDS: Convection; Instability; Cumulus clouds

1. Introduction

Shallow clouds organized into mesoscale patterns by convective instabilities have been recognized as a ubiquitous feature of the subtropical marine boundary layer since satellite imagery in the 1960s first revealed them (Agee et al. 1973). While their discovery sparked much research on the role of convective instabilities in patterning boundary layer clouds, much of that research was long focused toward open and closed convective cells (e.g., Fiedler 1985; Müller and Chlond 1996). Yet a rich spectrum of cloud patterns can be found outside the paradigm of such mesoscale cellular convection (Wood and Hartmann 2006), including for shallow cumulus clouds that top the trade wind marine boundary layer (Stevens et al. 2020; Denby 2020; Janssens et al. 2021).

The interest in the self-organization of trade wind cumulus has risen in recent years, in response to cloud-resolving simulations of deep convection (Muller and Held 2012), which spontaneously develop mesoscale fluctuations in their cloud structures. Since deep convective organization plays an important role in regulating radiative heat loss from the atmosphere (Tobin et al. 2012), it seemed natural to ask whether the observed shallow convective organization plays a similarly important role. Bony et al. (2020) suggest that the answer to this question is yes; in observations, different trade wind cumulus patterns, forming under different larger-scale conditions, have different cloud radiative effects. Given the disparity between observations and climate model simulations of the trade–cumulus feedback (Myers et al. 2021; Cesana and Del Genio 2021), this provides ample motivation for better understanding the processes that pattern shallow cumulus–topped marine boundary layers.

Many mesoscale cumulus patterns may simply be either passive responses to mesoscale heterogeneity in cloud-controlling conditions driven by larger-scale dynamics, or are remnants of extratropical disturbances advected into the trades (Schulz et al. 2021). However, several others appear to result from the shallow convection itself. Sub-cloud-layer rain evaporation can trigger density currents that force new convection upon collision (Seifert and Heus 2013; Zuidema et al. 2017), while heterogeneous radiative cooling can drive circulations (Naumann et al. 2019) that lead to cloud clustering (Klinger et al. 2017). Even simulations of clear convective boundary layers (Jonker et al. 1999) and stratocumulus-topped layers (de Roode et al. 2004) spontaneously develop appreciable mesoscale fluctuations in their moisture fields. Building on these studies, Bretherton and Blossey (2017, BB17 hereafter) in a remarkably thorough piece of work noted that even nonprecipitating shallow cumulus convection—stripped of all interactive precipitation and radiation feedbacks—self-organizes into clusters in large-eddy simulations (LESs) on domains larger than 100 km. More recently, Narenpitak et al. (2021) simulated a similar situation, and found their shallow cumuli grew horizontally at rates that correspond well to those observed in nature.

The recent discovery of length scale growth in nonprecipitating shallow cumulus convection is striking, since we have understood the basic premises of the slab-averaged structure of such convection since Riehl et al.'s (1951) observational budget surveys of the Northeast Pacific, the Atlantic Tradewind Experiment (ATEX;

Denotes content that is immediately available upon publication as open access.

Corresponding author: Martin Janssens, martin.janssens@wur.nl

DOI: 10.1175/JAS-D-22-0111.1

Augstein et al. 1973) and the Barbados Oceanographic and Meteorological Experiment (BOMEX; Nitta and Esbensen 1974): net condensation in a conditionally unstable cloud layer facilitates transport of liquid water into the trade inversion, where the condensate reevaporates. In a steady situation, this moistens and cools the inversion sufficiently to balance the drying and heating from the subsiding environment (Betts 1973, 1975), thus maintaining the trade wind boundary layer.

Using a minimal-physics LES of BOMEX, outlined in section 2, our first objective will be to use this classical view of the trade wind layer to show that the instability found by BB17 can be understood as a natural extension of the role played by net condensation in the slab mean (section 3) to mesoscale fluctuations around that mean (section 4). By predicating their mechanism on the well-understood basics of slab-averaged shallow cumulus convection, we hope to aid the interpretative side of future examinations, for instance attempts to understand the mechanism's relative importance to other processes that can pattern trade wind clouds.

Our second objective is to study the origins of the scale growth more quantitatively than BB17. To do so, we extend their theory to a linear stability model for bulk mesoscale moisture fluctuations, and examine its conditions for instability (section 5). We will show that these are satisfied by the cumulus convection itself, and do not require anything from the large-scale environment, other than that it supports a cumulus layer. Put differently, we will conclude that shallow cumulus convection is intrinsically unstable to length scale growth. We end the paper by discussing the relevance of these findings to several ongoing studies of the self-organizing cumulus layer, and suggest a few directions that such future research could take (section 6). A summary is given in section 7.

2. Large-eddy simulation of the undisturbed period during BOMEX

a. Case study

We consider a situation based on observations performed on 22 and 23 June 1969, during phase 3 of BOMEX. There are many reasons for this. First, during this so-called undisturbed period, the vertical slab-mean moisture and heat profiles were observed to be in a nearly steady state, capped by a well-defined inversion. In fact, the steadiness of these days was an important reason to select them for the budget studies that diagnosed the main features of cumulus convection in an undisturbed environment (Holland and Rasmusson 1973; Nitta and Esbensen 1974). Later, this also helped popularize the case as a test bed for validating LES models (Siebesma and Cuijpers 1995; Siebesma et al. 2003), as it allowed comparing statistics averaged over long time periods. As a result, the undisturbed period during BOMEX is perhaps the single most studied realization of the trade wind boundary layer. All these features make the situation attractive for our study, since it is our objective to use LES to study the development of fluctuations around a mean state that does not rapidly change, departing from the well-established theory from the early observational work.

It is worth pausing here to note that Nitta and Esbensen (1974) already show that the trade wind layer is usually not in a steady state, but is highly variable. Furthermore, recent observations of the subtropical Atlantic reveal that the trades usually feature stronger winds, weaker subsidence, and stronger temperature inversions than observed during the undisturbed period, often associated with larger-scale, precipitating cloud structures (Schulz et al. 2021). Therefore, the situation we study should be considered illustrative, rather than representative.

The second reason we concentrate on BOMEX is that BB17 also report LES results of the case. Their simulations produce significant mesoscale moisture and cloud fluctuations, if run for several days on domains whose horizontal dimensions exceed 100 km $\times$ 100 km. Hence, we will be able to translate rather directly between their results and ours.

Finally, the BOMEX setup we consider excludes and simplifies a number of processes. Of particular interest here are that the case (i) ignores spatial and temporal variability in the large-scale subsidence, horizontal wind and surface fluxes of heat and moisture, instead imposing steady and horizontally uniform forcings for all three, (ii) does not locally calculate radiative heating rates, instead approximating them with a slab-averaged cooling, and (iii) explicitly ignores the formation and impact of precipitation. This will suppress length scale growth encouraged by large-scale vertical ascent (Narenpitak et al. 2021), radiation (Klinger et al. 2017), and cold pools (Seifert and Heus 2013), respectively, all of which appear to be important pathways to develop the mesoscale cumulus patterns observed in nature.

We do not suggest that variable larger-scale forcing, radiation, and precipitation do not influence the length scale growth in shallow cumulus fields. We merely note that BB17 find that they are not necessary ingredients; they merely act to modulate an internal, dynamical growth mechanism that also occurs without them. The mechanism in question is thus fundamentally rooted in moist, shallow convection, and its understanding is clarified by only studying this aspect.

b. Model setup

We simulate BOMEX using the Dutch Atmospheric Large Eddy Simulation (DALES; Heus et al. 2010; Ouwersloot et al. 2017). We run the case precisely as reported by Siebesma et al. (2003), save for its computational grid, integration time and advection scheme. To allow the formation of mesoscale fluctuations with little influence from the finite domain size, the cases are run on horizontally square domains spanning 102.4 km, with a height of 10 km, for 36 h. The horizontal grid spacing $\Delta x = \Delta y = 200$ m, while the vertical grid spacing $\Delta z = 40$ m up to 6 km; it is stretched by 1.7% per level above this height. The case is run with a variance-preserving, second-order central difference scheme to represent advective transfer. We will concentrate our analysis on the early phase of the simulation, since it develops strong moisture fluctuations that approach the scale of the domain's horizontal size after around 18 h. Subsequently, deep convective clouds develop. Such situations are deemed unrealistic in our nonprecipitating simulations on domains with doubly periodic boundary conditions.

3. The classical theory

In the anelastic approximation adopted by our LES code, the local budget of a generic scalar χ, which here will denote water or a measure of heat, can be written as

$$\frac{\partial \chi}{\partial t} = -\frac{\partial}{\partial x_{\mathrm{jh}}}(u_{\mathrm{jh}}\chi) - \frac{1}{\rho_0}\frac{\partial}{\partial z}(\rho_0 w\chi) + S_\chi, \tag{1}$$

where u_{jh} contains the horizontal velocity vector, the subscript "jh" indicates summation over the horizontal coordinate, w is the vertical velocity, $\rho_0(z)$ is a profile of reference density, and S_χ is a local source. Since we are interested in fluctuations in χ, we introduce the definition

$$\chi = \overline{\chi} + \chi', \tag{2}$$

where $\overline{\chi}$ and χ' respectively refer to the slab average and resulting fluctuation of any model variable. It is instructive to use this partitioning to rewrite Eq. (1) on the following form (see appendix A for a step-by-step procedure):

$$\begin{aligned}\frac{\partial \chi}{\partial t} = &-\overline{u}_{\mathrm{jh}}\frac{\partial \chi}{\partial x_{\mathrm{jh}}} - u'_{\mathrm{jh}}\frac{\partial \overline{\chi}}{\partial x_{\mathrm{jh}}} - \frac{\partial}{\partial x_{\mathrm{jh}}}(u'_{\mathrm{jh}}\chi') - \overline{w}\frac{\partial \chi}{\partial z} - w'\frac{\partial \overline{\chi}}{\partial z}\\ &- \frac{1}{\rho_0}\frac{\partial}{\partial z}(\rho_0 w'\chi') + S_\chi,\end{aligned} \tag{3}$$

where we have used the anelastic conservation of mass. Equation (3) will serve as our point of departure for the rest of the study. In it, the first three terms describe horizontal transport (i) with the mean wind, (ii) with fluctuations in the horizontal velocity, and (iii) through turbulent fluxes, respectively. The fourth term represents transport with the mean vertical velocity, often associated with the prevailing subsidence of the trades, the fifth term denotes transport with vertical velocity fluctuations against the mean gradient, the sixth term describes vertical turbulent transport, and the final term is again reserved for sources.

a. Slab-averaged heat and moisture budgets

We will first briefly summarize the dynamics that govern the slab-averaged thermodynamic structure, since these dynamics turn out to also mostly explain the development of mesoscale fluctuations on top of it. The mean scalar budgets can be derived from Eq. (3) by (i) slab averaging it over a sufficiently large region to represent an ensemble average and (ii) assuming the horizontal flux divergence out of the region over which we average is small:

$$\begin{aligned}\underbrace{\frac{\partial \overline{\chi}}{\partial t}}_{\text{Tendency}} + \underbrace{\overline{u}_{\mathrm{jh}}\frac{\partial \overline{\chi}}{\partial x_{\mathrm{jh}}}}_{\text{Horizontal advection}} + \underbrace{\overline{w}\frac{\partial \overline{\chi}}{\partial z}}_{\text{Subsidence}} &= \underbrace{-\frac{1}{\rho_0}\frac{\partial}{\partial z}(\rho_0\overline{w'\chi'})}_{\text{Vertical flux convergence}}\\ + \underbrace{\overline{S_\chi}}_{\text{Sources}} &\equiv \underbrace{Q}_{\text{Apparent source}}\end{aligned} \tag{4}$$

Q defines Yanai et al.'s (1973) apparent heat source and moisture sink, if the equations are posed for appropriate heat and moisture variables, respectively. We will present these budgets for the two prognostic variables in our LES model, which are conserved under nonprecipitating cumulus convection: the total water specific humidity q_t and liquid-water potential temperature θ_l, approximated as

$$\theta_l \approx \theta - \frac{L_v}{c_p\Pi}q_l. \tag{5}$$

Here, $\theta = T/\Pi$ is (dry) potential temperature, T is temperature, L_v is the latent heat of vaporization, c_p is the specific heat of dry air at constant pressure, q_l is the liquid water specific humidity, and

$$\Pi = \left(\frac{p}{p_0}\right)^{R_d/c_p} \tag{6}$$

is the Exner function, with R_d the gas constant for dry air, p the reference pressure profile, and $p_0 = 10^5$ Pa.

In our LES model, which features doubly periodic boundary conditions, slab averages taken of horizontal gradients and vertical velocity are zero by definition. Therefore, we impose the horizontal transport and the vertical velocity in the subsidence term on the left-hand side of Eq. (4), in addition to a slab-averaged radiative cooling sink in the budget for θ_l. The resulting contributions to Eq. (4) are plotted in Figs. 1a and 1b; they mirror those simulated by Siebesma and Cuijpers (1995), which in turn reasonably match the apparent heat and moisture sources measured by Nitta and Esbensen (1974).

These budgets quantify the effects of shallow cumulus convection on the slab-average thermodynamic structure. It is characterized by a cloud layer, between the cloud base and a height we will call the inversion base, which is moistened and heated by the convergence of moisture and heat fluxes. Conversely, above the inversion base, the heat fluxes cool the layer until cloud top, countering the drying and warming from the mean environment's subsidence in what we will call the inversion layer. The imposed radiative source offers additional cooling throughout the layer. In spite of our intentions, and contrary to the models participating in Siebesma et al. (2003), these processes do not quite balance, resulting in a negative $\overline{\theta_l}$ tendency and positive $\overline{q_t}$ tendency in the inversion layer: our simulation does not approach a steady mean state for the long time series we simulate.

b. The role of net condensation

The appropriate thermodynamic quantity for analyzing the capacity of the boundary layer to work against the subsiding environment is the buoyancy. We will interpret buoyancy through fluctuations in virtual potential temperature θ_v:

$$\theta_v = \theta\left[1 + \left(\frac{R_v}{R_d} - 1\right)q_t - \frac{R_v}{R_d}q_l\right]. \tag{7}$$

Borrowing from Stevens (2007), these fluctuations can to good approximation be written as

$$\theta'_v \approx a_1\theta'_l + a_2\overline{\theta_l}q'_t + a_3\overline{\theta_l}q'_l, \tag{8}$$

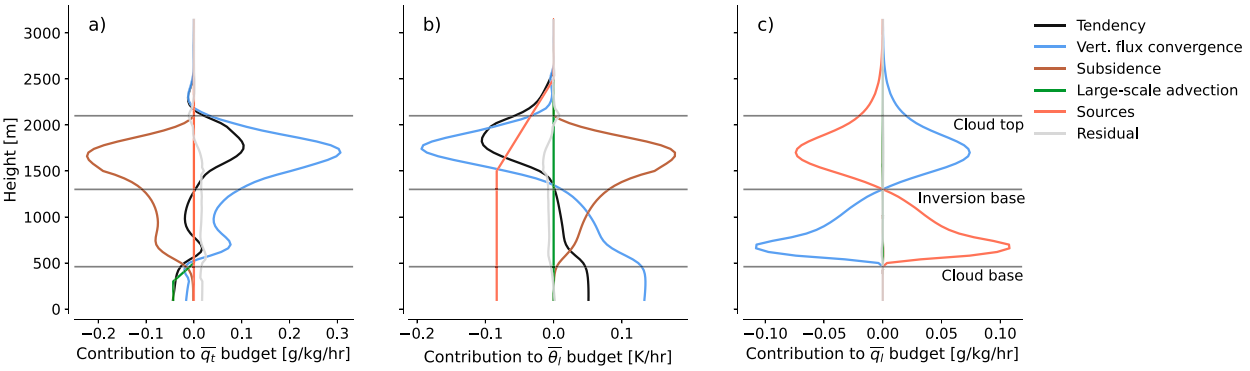

FIG. 1. Slab-averaged contributions to the slab-averaged tendencies of (a) q_t, (b) θ_l, and (c) q_l [Eq. (4) rewritten for $\partial\overline{\chi}/\partial t$ on the left-hand side], additionally averaged over hours 2–16 of the simulation. The source of $\overline{\theta_l}$ is radiative, negative, and imposed; the source of $\overline{q_l}$ is the net condensation rate.

with constants a_1–a_3 set to

$$a_1 = \frac{\theta_{v_c}}{\theta_{l_c}} \frac{1}{1 + \dfrac{q_{l_c} L_v}{c_p T_c}} \approx 1, \tag{9a}$$

$$a_2 = 1 - \frac{R_v}{R_d} \approx 0.608, \tag{9b}$$

$$a_3 = a_1 \frac{\theta_{l_c} L_v}{\theta_c c_p T_c} - \frac{R_v}{R_d} \approx 7. \tag{9c}$$

In these relations, cofluctuations among the thermodynamic variables are neglected, and θ_{v_c}, θ_{l_c}, θ_c, q_{l_c}, and T_c are taken to be representative cloud-layer constants; R_v is the ideal gas constant for water vapor. If we reinterpret the spatial fluctuations in Eq. (8) as changes occurring in time, we may also, to good approximation, write

$$\frac{\partial \theta_v}{\partial t} \approx \frac{\partial \theta_l}{\partial t} + a_2 \overline{\theta_l} \frac{\partial q_t}{\partial t} + a_3 \overline{\theta_l} \frac{\partial q_l}{\partial t}. \tag{10}$$

We will make two notes on Eq. (10) that prepare us for our subsequent discussion. First, $a_3 \overline{\theta_l}\, \partial q_l/\partial t$ is small in the slab average (Betts 1973), giving a powerful constraint that we return to in section 4d. Consider Eq. (4) with $\chi = q_l$, plotted in Fig. 1c. In our simulations, we do not impose large-scale horizontal transport of liquid water, while the effects of the prescribed subsidence on $\overline{q_l}$ are negligible. This simplifies Eq. (4) to

$$\frac{\partial \overline{q_l}}{\partial t} = -\frac{1}{\rho_0} \frac{\partial}{\partial z} (\rho_0 \overline{w' q_l'}) + \overline{\mathcal{C}} \approx 0, \tag{11}$$

where $\mathcal{C}$, the net condensation, is the only source in the absence of precipitation. Taken together, Eqs. (10) and (11) convey that net condensation is not stored ($\partial\overline{q_l}/\partial t \approx 0$) and does not contribute to building potential energy ($\partial\overline{\theta_v}/\partial t$). Instead, it is in the cloud layer rapidly exchanged into a liquid-water flux divergence; this is the balance shown in Fig. 1c. In the stable inversion layer, the transported liquid water entirely reevaporates, resulting in a convergence of $\overline{w' q_l'}$ that exactly balances the divergence in the cloud layer below.

Applying the constraint Eq. (11) to Eq. (10) brings us to our second note: Eq. (10) reduces to an equation for another quantity that is conserved in nonprecipitating convection, which Grenier and Bretherton (2001) call the liquid-water virtual potential temperature:

$$\theta_{lv} = \theta_l + a_2 \overline{\theta_l} q_t \equiv \theta_v - a_3 \overline{\theta_l} q_l. \tag{12}$$

Inserting Eq. (4) with $\chi \in [\theta_l, a_2 \overline{\theta_l} q_t]$ in the slab-averaged Eq. (10) gives

$$\frac{\partial \overline{\theta_v}}{\partial t} \approx \frac{\partial \overline{\theta_{lv}}}{\partial t} = -\frac{1}{\rho_0} \frac{\partial}{\partial z} [\rho_0 (\overline{w' \theta_l'} + a_2 \overline{\theta_l} \overline{w' q_t'})] - \overline{u_{jh}} \frac{\partial \overline{\theta_{lv}}}{\partial x_{jh}} - \overline{w} \frac{\partial \overline{\theta_{lv}}}{\partial z} + \overline{S_{\theta_{lv}}}, \tag{13}$$

from which we may observe the consequence of the assumption that liquid water storage is small [Eq. (11)]: the tendency of $\overline{\theta_v}$ depends not on the slab-averaged buoyancy flux $\overline{w' \theta_v'}$, but on fluxes of θ_{lv}, which may be derived from Eq. (8) by multiplication with w':

$$w' \theta_{lv}' = w' \theta_l' + a_2 \overline{\theta_l} w' q_t' \equiv w' \theta_v' - a_3 \overline{\theta_l} w' q_l'. \tag{14}$$

The slab average of this flux and its contributions are plotted in Fig. 2; this figure largely explains the effect of $\mathcal{C}$ on the layer. In one view of Eq. (14), the structure of $\overline{w' \theta_{lv}'}$ (maroon line) closely follows that of $\overline{w' \theta_l'}$ (yellow line). However, one may use Eq. (5) to write

$$w' \theta_l' = w' \theta' - \frac{L_v}{c_p \Pi} w' q_l', \tag{15}$$

which led Betts (1975) to recognize that it is mainly the liquid-water flux contribution (blue line) that is responsible for maintaining the large, downward $\overline{w' \theta_l'}$ in the cloud layer. The other view of Eq. (14) follows Stevens (2007): $w' \theta_{lv}'$ is the buoyancy flux, minus its contributions from liquid water fluxes. By definition, $w' \theta_v' = w' \theta_{lv}'$ in the subcloud layer. But in the cloud layer, Fig. 2 shows how the former is substantially

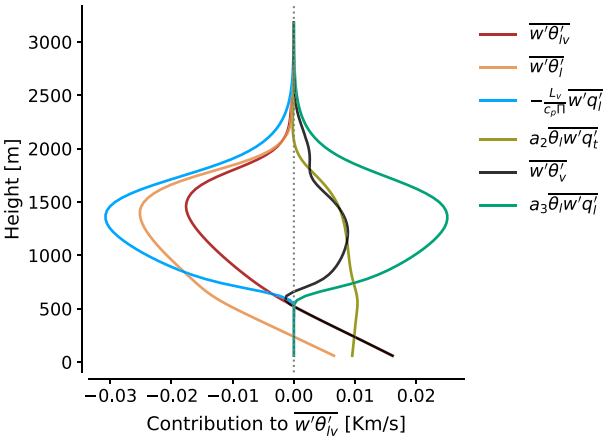

FIG. 2. Contributions of the fluxes in Eqs. (14) and (15) to $\overline{w'\theta'_{lv}}$, averaged over hours 6–16 of the simulation.

outweighed by the latter. In both views, the structure of $\overline{w'\theta'_{lv}}$ is mainly supported by that of $\overline{w'q'_l}$. Since Eq. (11) shows how $\mathcal{C}$ governs the net divergence of $\overline{w'q'_l}$ in the cloud layer and its convergence in the inversion layer, this discussion buttresses the classical picture of the cumulus-topped boundary layer that we drew in the introduction: net condensation in the cloud layer, and the subsequent transport to, reevaporation in, and cooling of the inversion layer, oppose the net heating of the subsiding environment, and thus maintain the structure of $\overline{\theta_v}$ across the trade inversion.

4. Summary of BB17's model for mesoscale fluctuations

We are now ready to summarize BB17's model for the development of mesoscale fluctuations. We will do so using only the classical theory outlined above, and a single assumption on the horizontal buoyancy field that also turns out to have similar consequences as we have already discussed. In section 5, we will then move beyond BB17's theory, to a closed-form model of the instability and an analysis of its conditions.

a. Definitions

Following BB17, we will frame length scale growth in our fields as an increase in magnitude of mesoscale fluctuations that develop over the slab average. One can identify such mesoscale fluctuations in χ by partitioning χ', defined in Eq. (2), into a mesoscale component χ'_m and submesoscale component χ'_s, which gives

$$\chi = \overline{\chi} + \chi'_m + \chi'_s. \tag{16}$$

BB17 scale partition their variables by extracting horizontal averages over blocks of 16 km × 16 km. Here, we conduct the decomposition with a spectral low-pass filter at the horizontal wavenumber that corresponds to scales of 12.5 km. As an example, consider Fig. 3; our spectral filter extracts the field shown in the right panel from that shown in the left panel. Of course, any choice of method and scale for this separation is somewhat arbitrary. Yet, since the filter's primary objective is to distinguish mesoscale fluctuations from fluctuations that occur on the scale of a typical cumulus cloud, any consistently performed scale separation at a scale that is larger than this typical cumulus scale (around 1 km), but sufficiently smaller than our finite domain size (100 km), suffices to illustrate what we intend to show. We also find that no aspect of the upcoming analysis meaningfully changes if we filter at wavenumbers corresponding to 6.25 or 25 km.

In the following, special attention will be paid to "moist, mesoscale regions." To define such regions, we use the density-weighted vertical average

$$\langle \chi \rangle = \frac{\int_0^{z_\infty} \rho_0 \chi dz}{\int_0^{z_\infty} \rho_0 dz}, \tag{17}$$

where z_∞ refers to the domain top at 10 km. From this follows a definition of the column-averaged, or bulk moisture $\langle q_t \rangle$. We will take moist mesoscale regions to be horizontal coordinates

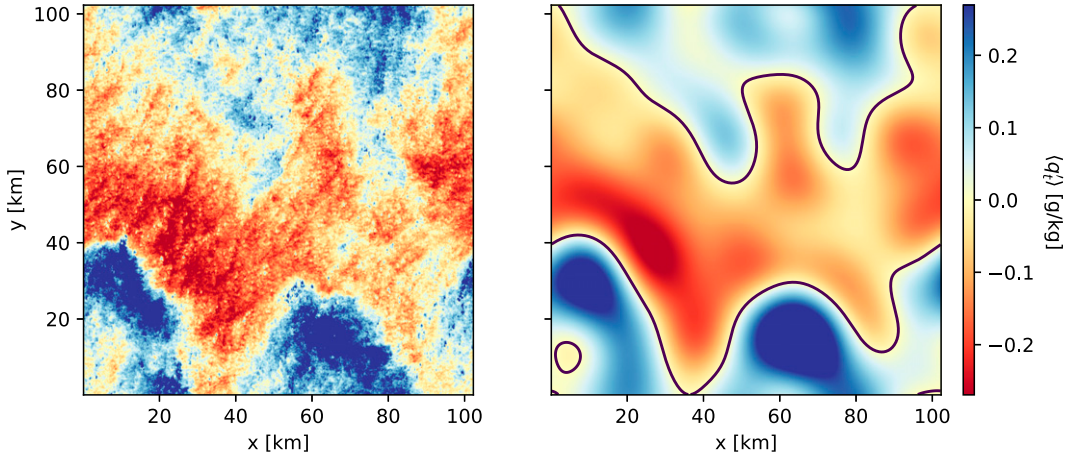

FIG. 3. (left) Fluctuations of column-averaged total specific humidity q'_t and (right) its mesoscale-filtered component $\langle q'_{t_m} \rangle$, overlaid with a contour separating mesoscale regions that are moister and drier than the spatial mean after 24 h.

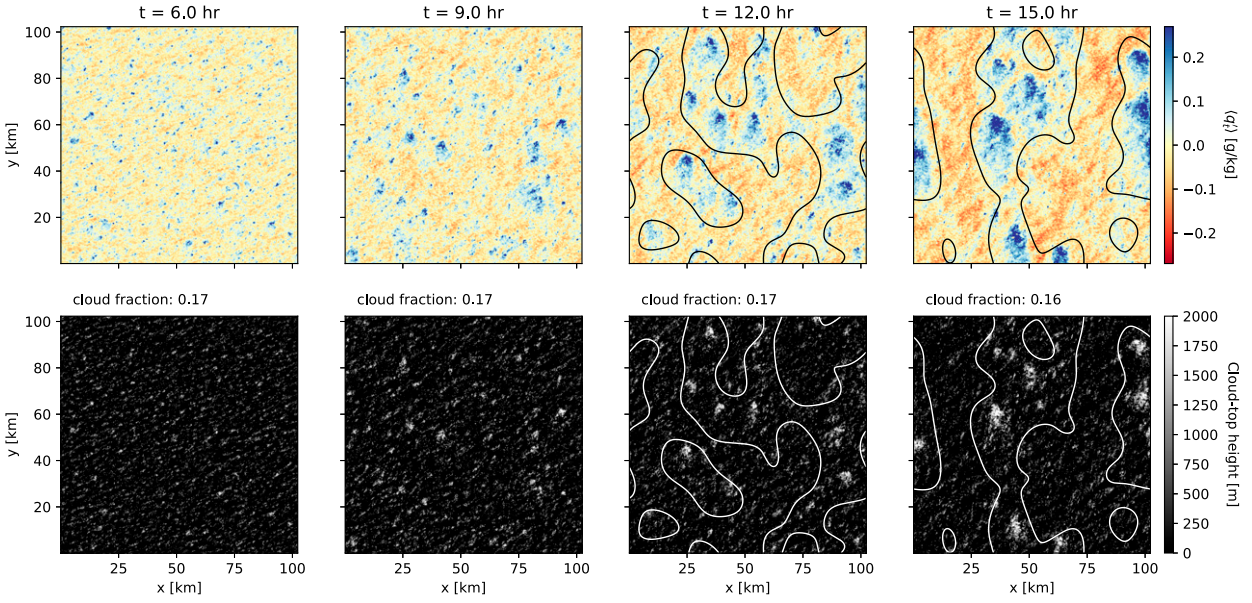

FIG. 4. Time evolution (left to right) of (top) $\langle q'_{t_m} \rangle$ and (bottom) cloud-top height, overlaid by contours that separate moist and dry mesoscale regions at 12 and 15 h, and annotated with cloud fraction.

where $\langle q'_{t_m} \rangle > 0$, and dry mesoscale regions where $\langle q'_{t_m} \rangle < 0$. The black contour line in the right panel of Fig. 3 gives a visual impression of this delineation.

With these definitions, we formulate a budget for χ'_m, by subtracting Eq. (4) from Eq. (3), making several assumptions that make the equation consistent with our LES, mesoscale filtering the result, and rearranging the terms (see appendix A for the derivation's details):

$$\frac{\partial \chi'_m}{\partial t} = -w'_m \Gamma_\chi - \frac{1}{\rho_0}\frac{\partial}{\partial z}(\rho_0 F_{\chi'_m}) - \frac{\partial}{\partial x_{\mathrm{jh}}}(u_{\mathrm{jh}}\chi')_m - \overline{w}\frac{\partial \chi'_m}{\partial z} + S'_{\chi_m}. \tag{18}$$

In this relation, we define $\partial\overline{\chi}/\partial z = \Gamma_\chi$ and

$$F_{\chi'_m} = (w'\chi')_m - \overline{w'\chi'}, \tag{19}$$

i.e., the anomalous mesoscale-filtered vertical flux of χ' away from the slab average.

In spite of the number of steps taken to derive it, we draw attention to Eq. (18)'s similarity to the slab-averaged budget, Eq. (4). It features the vertical and horizontal convergence of χ'_m [second and third terms on the right-hand side of Eq. (18), respectively], the mesoscale anomalous effect of subsidence (fourth term) and sources (fifth term). The most important difference with Eq. (4) is the first term, which describes transport along the mean gradient of χ with mesoscale vertical velocity fluctuations. This term will prove to be central.

Many of our results will show averages of Eq. (18) over moist and dry mesoscale regions, which, because such regions are not entirely stationary, introduces two nuances to the horizontal transport term (see appendix A). First, we remove horizontal mean flow advection of the mesoscale fluctuations and consider only the net horizontal transport from one region to another. Second, we must account for a divergence term that describes the net expansion of the regions themselves, with velocity u^e_{jh}. Denoting averages over moist or dry regions by $\tilde{\cdot}$, this finally gives

$$\underbrace{\frac{\partial \widetilde{\chi'_m}}{\partial t}}_{\text{Tendency}} = \underbrace{\widetilde{-w'_m}\Gamma_\chi}_{\text{Gradient production}} - \underbrace{\frac{\partial}{\partial x_{\mathrm{jh}}}\widetilde{(u'_{\mathrm{jh}}\chi')_m}}_{\text{Cross-region transport}} + \underbrace{\frac{\partial}{\partial x_{\mathrm{jh}}}\widetilde{(u^e_{\mathrm{jh}}\chi')_m}}_{\text{Expansion}} - \underbrace{\frac{1}{\rho_0}\frac{\partial}{\partial z}\widetilde{(\rho_0 F'_{\chi_m})}}_{\text{Vertical transport}} - \underbrace{\overline{w}\frac{\partial \widetilde{\chi'_m}}{\partial z}}_{\text{Subsidence}} + \underbrace{\widetilde{S'_{\chi_m}}}_{\text{Source}}. \tag{20}$$

To keep the text uncluttered, we will only discuss explicitly regions where $\langle q'_{t_m} \rangle > 0$, since observations pertaining to such regions are generally the opposite in dry, mesoscale regions, albeit of different magnitude. To give the reader an impression of this asymmetry, the figures will generally present both moist and dry profiles.

b. A sketch of the instability

The top row of Fig. 4 shows how small disturbances in $\langle q'_t \rangle$ grow into significant mesoscale fluctuations over an 8 h time window. The figure's bottom row identifies growing clusters of shallow cumulus clouds that develop on top of these mesoscale regions, becoming more vigorous and reaching deeper into the inversion as they grow. Since the mesoscale fluctuations in the temperature variables discussed in section 3 remain small with respect to their root-mean-square (see Figs. 5d–f), this suggests that to understand the length scale growth of our clouds, we must understand what drives the formation of $\langle q'_{t_m} \rangle$.

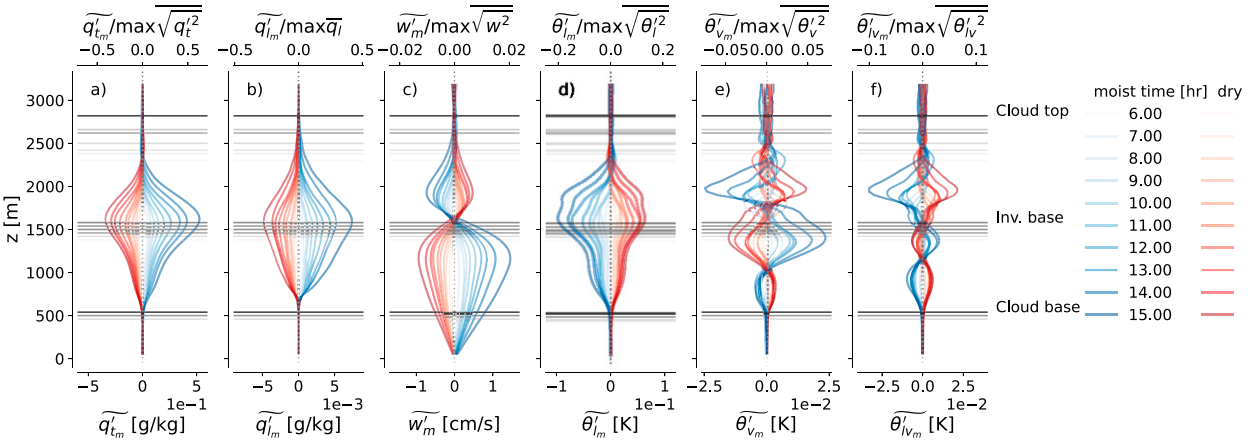

FIG. 5. Time evolution of mesoscale fluctuations, averaged over moist and dry mesoscale regions for (a) total specific humidity q_t, (b) liquid-water specific humidity q_l, (c) vertical velocity w, (d) liquid-water potential temperature θ_l, (e) virtual potential temperature θ_v, and (f) liquid-water virtual potential temperature θ_{lv}. Upper axes indicate the maximum of these fluctuations relative to the maximum root-mean-square fluctuation in each quantity at the last, plotted time.

Figure 6 offers a sketch of the explanation. Over the vertical dimension, clouds (black contour lines) develop favorably on top of a patch of $q'_{t_m} > 0$ (black, dashed contour) in the upper cloud layer. The q'_{t_m} structure is produced by a mesoscale circulation ascending at approximately 1 cm s^{-1} (overlaid streamlines), which converges in the subcloud layer beneath the structure, transports moisture upward along the negative, slab-mean vertical moisture gradient, and detrains it laterally near the inversion base around 1500 m, where the mesoscale vertical velocity w'_m becomes negative. Figure 5, which shows the temporal development of mesoscale fluctuations in q_t, q_l, and w'_m, averaged over moist and dry mesoscale regions, quantifies these statements. The reader will recognize that we have here merely described the action of the first term in Eqs. (18) and (20); we will make this connection explicit in section 4c.

The mesoscale circulations themselves arise from corresponding mesoscale variations in the classical theory of the slab-averaged layer that we have discussed in section 3, supplemented by a single, well-known assumption from mesoscale tropical meteorology, namely, that horizontal fluctuations in density remain small. We observe the resulting "weak temperature gradients" in the profiles of mesoscale buoyancy fluctuations θ'_{v_m}, plotted in Fig. 5e, which do not differ appreciably between moist and dry mesoscale regions. This allows the circulations to develop directly from mesoscale fluctuations in work done by condensation anomalies in the cloud layer, and matching evaporation anomalies in the inversion layer; we show this in section 4d. With reference to our discussion in section 3, such energy fluctuations are anticipated by the mesoscale-filtered vertical flux of liquid water in Fig. 6

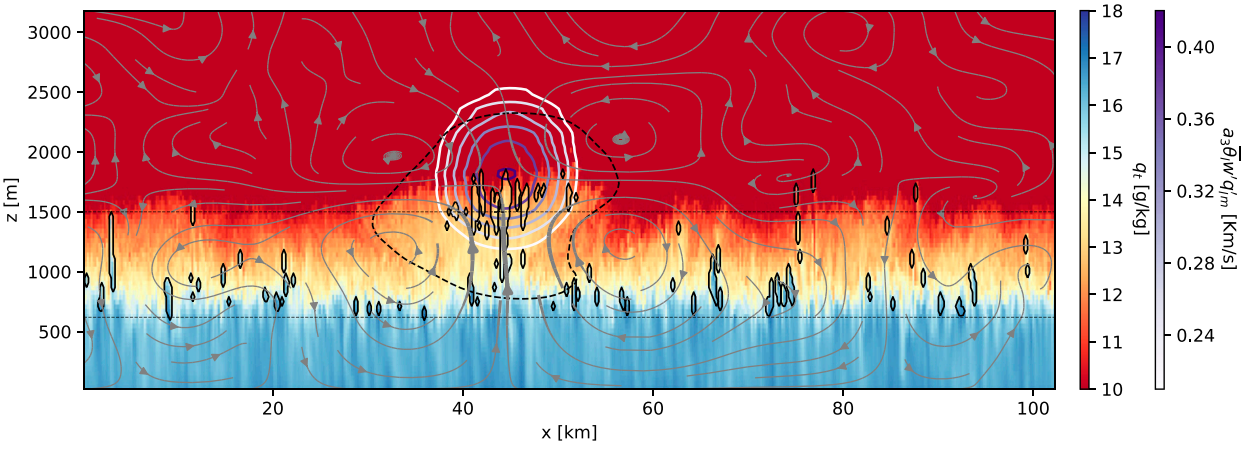

FIG. 6. Cross section over an example y–z plane of our simulation at 16 h, colored by filled contours of q_t (red to blue) and overlaid by contour lines of (i) $\langle q'_{t_m} \rangle > 0$ (black dashed), (ii) clouds (black solid), and (iii) $(w'q'_l)_m$ (white to blue; it does not coincide with the clouds because it is mesoscale filtered at slab level). Also overlaid are streamlines of the mesoscale-filtered, in-plane velocity fluctuations [defined by (u'_m, w'_m)], whose line thickness is weighted by this velocity's local magnitude. Horizontal dashed lines represent cloud base and inversion base.

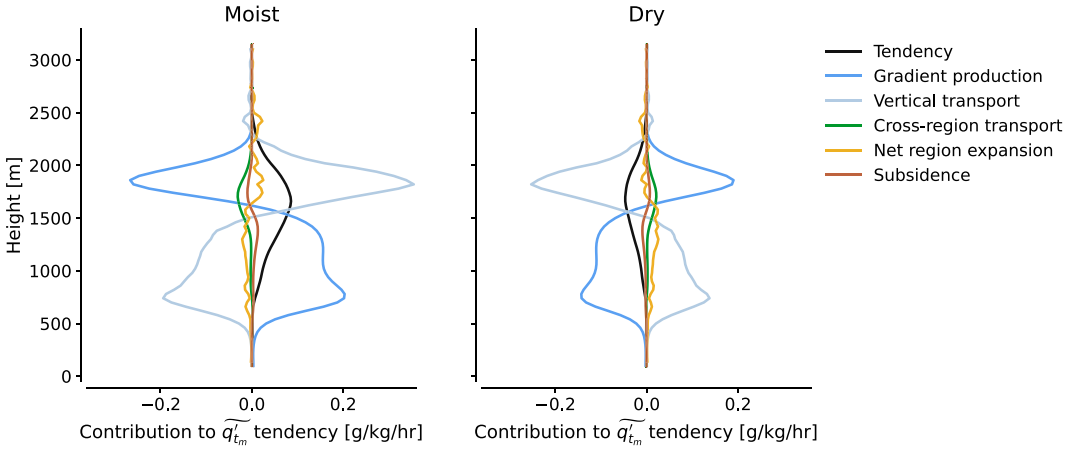

FIG. 7. Vertical profiles of the terms in the q'_{t_m} budget averaged over moist and dry mesoscale regions [Eq. (20)], and over 10–16 h.

(white-to-blue contours) scaled to units of virtual potential temperature transport.

The mesoscale condensation anomalies again favor regions with positive mesoscale moisture fluctuations, which control the mesoscale relative humidity fluctuations when the (potential) temperature fluctuations, shown in Figs. 5d–f, are small. In all, BB17 then identify a self-reinforcing feedback: mesoscale fluctuations in condensation and evaporation in cumulus clouds give rise to mesoscale circulations, which in turn enhance mesoscale moisture fluctuations, on top of which stronger mesoscale fluctuations in condensation and evaporation develop.

c. *Mesoscale moisture fluctuations develop from mesoscale circulations*

Figure 7 shows the terms in Eq. (20) with $\chi = q_t$. It identifies the main reason for the rise of $q'_{t_m} > 0$ in the moist cloud layer to be the production of q'_{t_m} by vertical, mesoscale transport along the mean, negative moisture gradient Γ_{qt}. We will call this "gradient production," in the spirit of variance-budget studies (e.g., de Roode et al. 2004; Heinze et al. 2015; Anurose et al. 2020), which show that this term, when scaled with the moisture fluctuation itself, is the main driver of moisture variance in cloud-topped boundary layers. Our gradient production essentially quantifies a similar process as variance production, but confines it to the mesoscale. The term follows directly from the w'_m profiles plotted in Fig. 5c, which Fig. 6 revealed to capture the ascending and descending branches of spatially coherent mesoscale circulations. w'_m becomes increasingly positive in the moist cloud layer, and increasingly negative in the moist inversion layer, accelerating the gradient production in time.

Figure 7 also shows that the largest local opponent to the gradient production of q'_{t_m} is the convergence of anomalous vertical moisture fluxes. These fluxes transport the positive moisture fluctuation that is produced in the moist cloud layer into the overlying inversion. Since the term's vertical integral is zero under the homogeneous flux condition we impose on our lower boundary, it does not add or remove $\langle q'_{t_m} \rangle$ from a column; it just translates the vertical structure of $-w'_m \Gamma_{qt}$ into profiles of its tendency (black line in Fig. 7). It is therefore also mainly responsible for situating the peak of the mesoscale fluctuations in cloudiness (q'_{t_m}, see Fig. 5b) near the inversion base, and not near cloud base.

Horizontal transport enters the budget through (i) the mesoscale horizontal moisture fluxes from moist to dry mesoscale regions (cross-regional transport) and (ii) the net region expansion with u^e_{jh}. The net region expansion is generally small (yellow line), though it tends negative in the moist cloud layer, where the converging circulation acts to concentrate q'_{t_m}, and positive in the inversion, where the diverging circulation acts to expand the region boundary. These effects are generally outweighed by inversion-drying from transport across the region boundary (olive line) with the mesoscale flow and through turbulent mixing of q'_{t_m} down the horizontal moisture gradient, both of which draw q'_{t_m} from the mesoscales.

The subsidence term is a small direct contributor to the budget; as we have seen, its primary role is in setting the slab-mean environment in which the moisture fluctuations can develop. The budget has no further sources, i.e., in the absence of precipitation, $S'_{q_{t_m}} = 0$.

The relative importance of the gradient production and horizontal transport of q'_{t_m} to the development of moist and dry mesoscale regions is adequately captured by vertically averaging Eq. (20) with $\chi = q_t$ using Eq. (17), which gives a budget for $\langle q'_{t_m} \rangle$; the time evolution of this budget is plotted in Fig. 8. It shows that the column-averaged mesoscale moistening rate increases roughly exponentially in moist areas, and that it is initially well-approximated by the gradient production. Only once significant mesoscale moist patches have formed (see Fig. 4 at 12 and 15 h) do horizontal fluxes begin substantially opposing it. This suggests that the onset of growth in q'_{t_m} is production driven, while the horizontal structure and later development of the fluctuations also depend on the efficiency with which horizontal transport can redistribute them.

The net expansion's column average is small, but slightly negative in moist areas; i.e., not only are large, moist areas becoming moister, they are also becoming slightly smaller. We

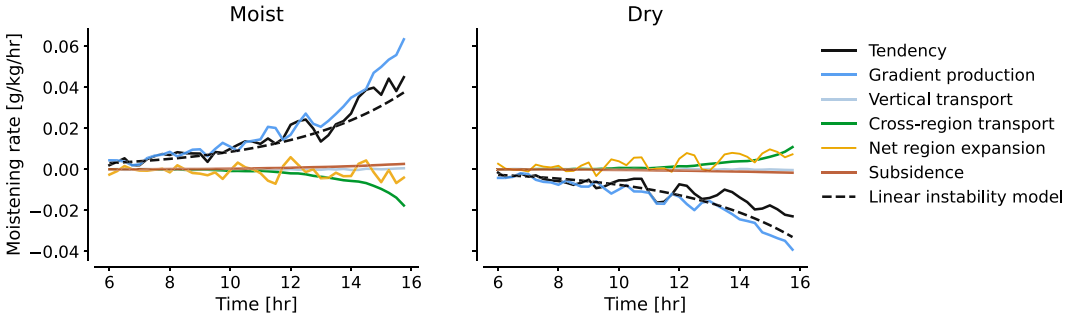

FIG. 8. Time evolution of the $\langle q'_{t_m} \rangle$ budget [Eq. (17) applied to Eq. (20)], averaged over moist and dry mesoscale regions, between 6 and 16 h, in the spirit of Fig. 13 of BB17. The dashed line plots the linear instability Eq. (30).

will briefly discuss this clustering tendency and its significance in section 6.

d. *Mesoscale circulations develop from anomalous condensation in clouds*

1) WEAK TEMPERATURE GRADIENTS

To understand why moist mesoscale regions become moister, we must deduce the source of w'_m in the gradient production of q'_{t_m}. In other words, why does the mesoscale circulation shown in Fig. 6 develop? BB17 argue that this is best understood through a weak temperature gradient (WTG) framework (e.g., Held and Hoskins 1985; Sobel et al. 2001), which has proven useful in explaining self-organized, circulation-driven scale growth in the moisture fields of tropical atmospheres in radiative–convective equilibrium (e.g., Emanuel et al. 2014; Chikira 2014; Beucler et al. 2018; Ahmed and Neelin 2019).

While deep convective clouds are the most spectacular example, any sort of convection in a stably stratified fluid generates density fluctuations which gravity waves continually redistribute horizontally, also the shallow cumuli under consideration here. Since these waves travel at a characteristic speed much higher than that with which advection can transport mixed scalars such as moisture, they may prevent buoyancy fluctuations from accumulating over the time scale with which q'_{t_m} grows; i.e., the mesoscale buoyancy fluctuations remain small. A WTG interpretation of the governing equations then allows using the mesoscale buoyancy budget to diagnose w'_m.

To understand this, we first mesoscale filter our definition for buoyancy [Eq. (8)]:

$$\theta'_{v_m} = \theta'_{l_m} + a_2 \overline{\theta_l} q'_{t_m} + a_3 \overline{\theta_l} q'_{l_m}. \tag{21}$$

From Eq. (21), it is not immediately obvious that θ'_{v_m} should be small. For instance, if $\theta'_{l_m} \approx 0$, $\theta'_{v_m} \approx \overline{\theta_l}(a_2 q'_{t_m} + a_3 q'_{l_m})$. So, upon inspecting Figs. 5a and 5b, one may expect to find mesoscale buoyancy fluctuations that correlate to the moisture and liquid water fluctuations. This turns out to be a very good approximation in layers of relatively continuous cloud cover, such as closed cell convection (de Roode et al. 2004; de Roode and Los 2008), in which thermals hardly penetrate the stable layer above the mixed layer and thus give gravity waves much less of a chance to redistribute their buoyancy. In such situations, significant θ'_{v_m} are observed to develop in the cloud layer, which may contribute directly to the development of w'_m through the mesoscale-filtered vertical momentum equation.

However, our broken cumulus layer demands a different view: Fig. 9, which plots the contributions to Eq. (21) (opaque lines) and their time evolution (increasingly dark, transparent lines), indicates $\widetilde{\theta'_{l_m}} \neq 0$ and $a_2 \overline{\theta_l} \widetilde{q'_{t_m}} \gg a_3 \overline{\theta_l} \widetilde{q'_{l_m}}$. Instead of remaining small, θ'_{l_m} becomes increasingly negative in moist mesoscale regions, while $a_3 \overline{\theta_l} \widetilde{q'_{l_m}}$ remains almost negligible. The result is an approximate balance between the θ'_{l_m} and q'_{t_m} contributions in Eq. (21), and a comparatively small $\widetilde{\theta'_{v_m}}$ (black line in Fig. 9) with little temporal development. Hence, if we differentiate Eq. (21) to time, we may write the mesoscale-fluctuation equivalent of Eq. (10), and recognize that it is stationary, akin to its slab-averaged counterpart being steady to maintain a stable trade inversion:

$$\frac{\partial \theta'_{v_m}}{\partial t} = \frac{\partial \theta'_{l_m}}{\partial t} + a_2 \overline{\theta_l} \frac{\partial q'_{t_m}}{\partial t} + a_3 \overline{\theta_l} \frac{\partial q'_{l_m}}{\partial t} \approx 0. \tag{22}$$

Equation (22) is our statement of the WTG approximation. Before using it, we pause to employ the observation that the temporal development of $a_3 \overline{\theta_l} \widetilde{q'_{l_m}}$ does not seem to appreciably influence $\widetilde{\theta'_{v_m}}$ (Fig. 9). Indeed, we may approximate Eq. (18) for q_l as a slightly more stringent version of Eq. (11):

$$\frac{\partial q'_{l_m}}{\partial t} \approx -\frac{\partial}{\partial z}(F_{q'_{l_m}}) + \mathcal{C}'_m \approx 0. \tag{23}$$

Hence, in another parallel of the slab-mean theory, mesoscale anomalies in the rate of net condensation $\mathcal{C}$ are approximately balanced by anomalies in their vertical transport, represented by the divergence of $F_{q'_{l_m}}$, making storage of q'_{l_m} passive in our dynamics. These assumptions are confirmed by Fig. 10.

The upshot of this discussion is that even though we in section 3 posed budgets for θ_v to analyze the stability of the trade wind layer's slab-averaged structure to vertical growth, while we here pose it to analyze the growth of horizontal fluctuations, the consequences of applying Eq. (23) are similar: Eq. (22) again reduces to a budget for θ_{lv}, only here for its mesoscale fluctuations. Because Eq. (23) holds, θ'_{lv_m} satisfies the WTG

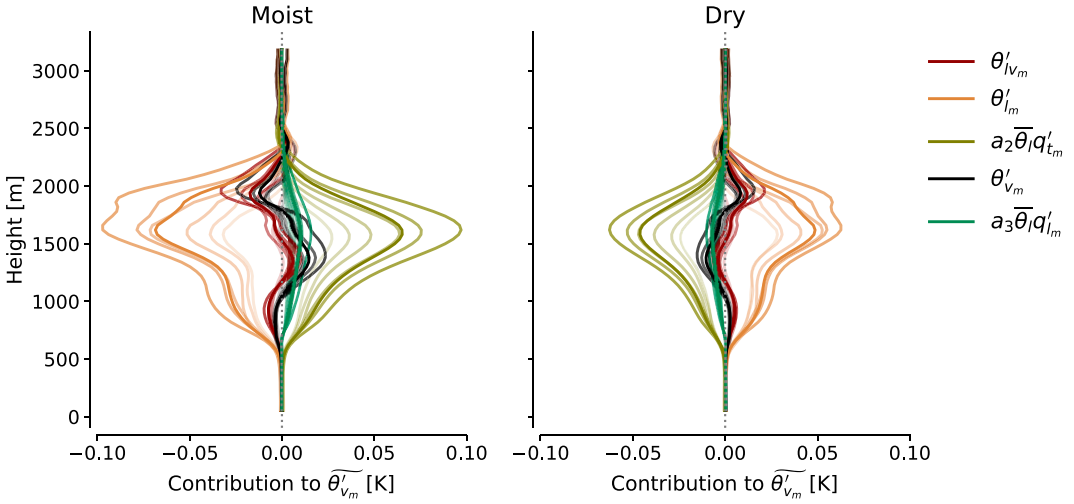

FIG. 9. Vertical profiles of θ'_{v_m} [Eq. (8)] and θ'_{lv_m} [Eq. (12)], and their contributions from θ'_{l_m}, q'_{t_m}, and q'_{l_m}, averaged over (left) moist and (right) dry mesoscale regions, over 10–16 h (dark lines) and over every hour between 10 and 16 h (transparent lines, in order of increasing opacity).

approximation as well as θ'_{v_m}. In adopting it, we again follow BB17, who perform their analysis in terms of liquid virtual static energy, the energy equivalent to θ_{lv}.

2) MODELING w'_m

The budget for θ'_{lv_m} follows from inserting the (scaled) tendencies of θ'_{l_m} and q'_{t_m}, as written in Eq. (22), into Eq. (18). Subsuming transport and sources of θ'_{lv_m} under $S'_{\theta_{lv_m}}$ then gives the WTG formulation on a commonly written form:

$$\frac{\partial \theta'_{lv_m}}{\partial t} = -w'_m \Gamma_{\theta_{lv}} + S'_{\theta_{lv_m}} \approx 0. \tag{24}$$

Figure 11 plots all terms in this budget, averaged over moist and dry regions. It reveals that the gradient production is primarily balanced by anomalous, vertical mesoscale convergence of θ'_{lv} fluxes ($F_{\theta'_{lv_m}}$); both terms are at least an order of magnitude larger than θ'_{lv_m}'s tendency, horizontal advection, and subsidence heating. Hence, the figure invites us to rewrite Eq. (24) as a diagnostic equation for w'_m, which can be understood as the vertical velocity needed to move air parcels heated by $S'_{\theta_{lv_m}}$ quasi statically to their level of neutral buoyancy under a stable stratification (Klein 2010). In our nonprecipitating simulations with homogeneous, imposed radiation, the anomalous heat source $S_{\theta'_{lv_m}}$ is reduced to the vertical convergence of $F_{\theta'_{lv_m}}$. Hence, the model reads

$$w'_m \approx -\frac{1}{\rho_0}\frac{\partial}{\partial z}(\rho_0 F_{\theta'_{lv_m}})\frac{1}{\Gamma_{\theta_{lv}}}. \tag{25}$$

Figures 12a and 12b confirm the accuracy of this approximation, except in the well-mixed subcloud layer, where $\Gamma_{\theta_{lv}}$ becomes small.

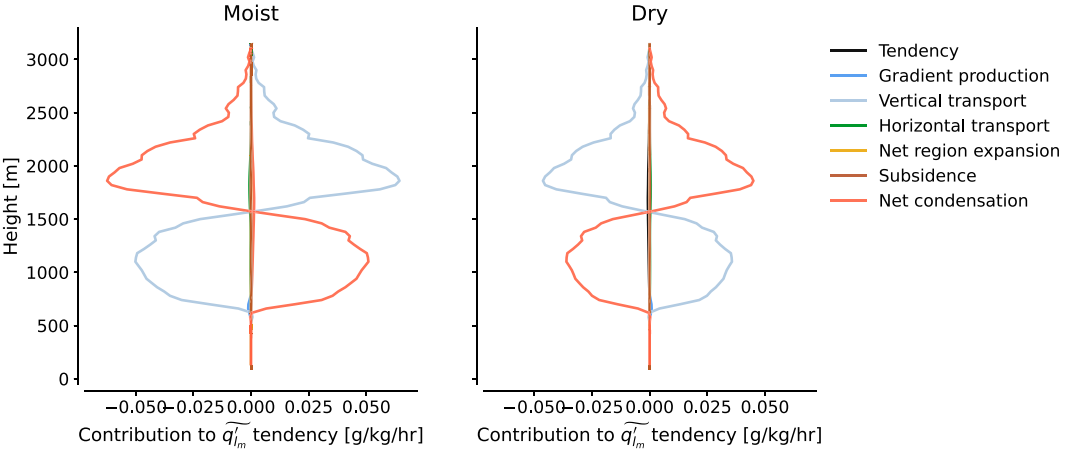

FIG. 10. Vertical profiles of the terms in the q'_{l_m} budget averaged over (left) moist and (right) dry mesoscale regions [Eq. (20), which approximately reduces to Eq. (23)] and over 10–16 h.

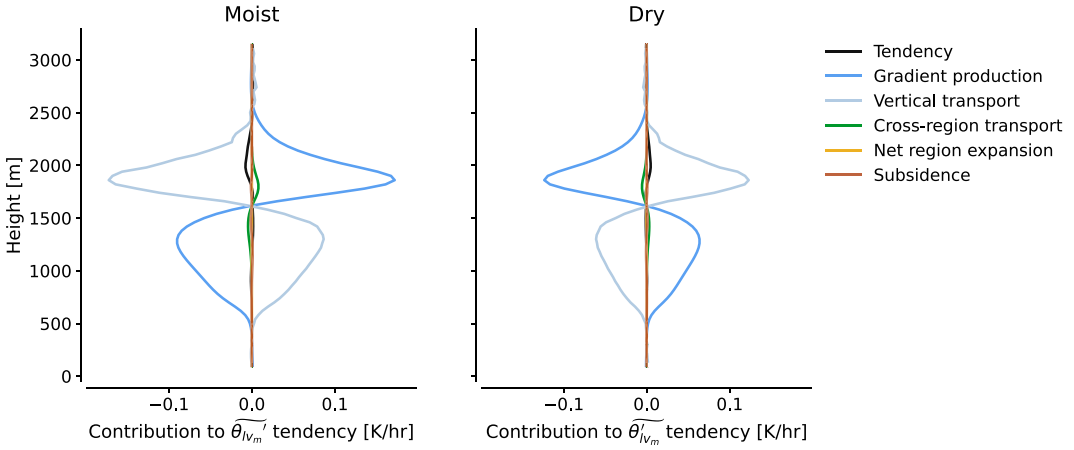

FIG. 11. Vertical profiles of the terms in the θ'_{lv_m} budget [Eq. (20), which approximately reduces to Eq. (24)], averaged over (left) moist and (right) dry mesoscale regions and over 10–16 h.

3) THE ROLE OF CONDENSATION

What governs the vertical convergence of $F_{\theta'_{lv_m}}$? Figure 11 shows that it is positive in the moist region's cloud layer, and negative in the corresponding inversion layer. To explain this, we will for a final time return to our discussion from section 3.

Figure 13 plots the mesoscale-filtered and slab-averaged contributions to $w'\theta'_{lv}$, obtained from mesoscale filtering Eq. (14), and compares them to the slab-averaged fluxes previously presented in Fig. 2. The vertical structure of the fluxes in the cloud layer is qualitatively similar when averaging them over either the entire slab, the moist mesoscale regions, or the dry mesoscale regions; they only differ in their magnitude. Therefore, just like we found the structure of $\overline{w'\theta'_{lv}}$ to be facilitated by that of $\overline{w'q'_l}$, we recognize that the structure of $(w'\theta'_{lv})_m$ is facilitated by that of $(w'q'_l)_m$, when averaged over moist and dry regions. This is possible in spite of $\theta'_{lv_m} \approx \theta'_{v_m}$ throughout the boundary layer (Fig. 9), because Eq. (23) shows that mesoscale condensation anomalies do not accumulate as q'_{l_m}, but instead give rise to an anomalous divergence of liquid water flux in the moist cloud layer. The contribution from q'_{l_m} to θ'_{lv_m} [Eq. (21)] is small; the contribution from $(w'q'_l)_m$ to $(w'\theta'_{lv})_m$ [filtered Eq. (14)] is not.

In moist regions, Fig. 13 shows that $F_{q'_{l_m}} > 0$. Using Eq. (23), we recognize this to result directly from $\mathcal{C}'_m > 0$. Put differently, the heating $-\partial F_{\theta'_{lv_m}}/\partial z$ in the left panel of Fig. 11 is to good approximation the mesoscale projection of anomalous work done by condensation at the cumulus scale. Equation (25) then shows that this heating is immediately compensated by mesoscale ascent along the mean stratification, as mandated by the WTG model. As a result of the slab-mean-exceeding liquid water transport from the layer below, the moist inversion layer must also evaporate more liquid water than the slab average, i.e., $\mathcal{C}'_m < 0$. Consequently, the moist inversion layer experiences an anomalous convergence of $(w'q'_l)_m$ and an associated anomalous cooling, i.e., $-\partial F_{\theta'_{lv_m}}/\partial z < 0$ in Fig. 11. Just like in the cloud layer below, this cooling is quickly balanced by a negative w'_m.

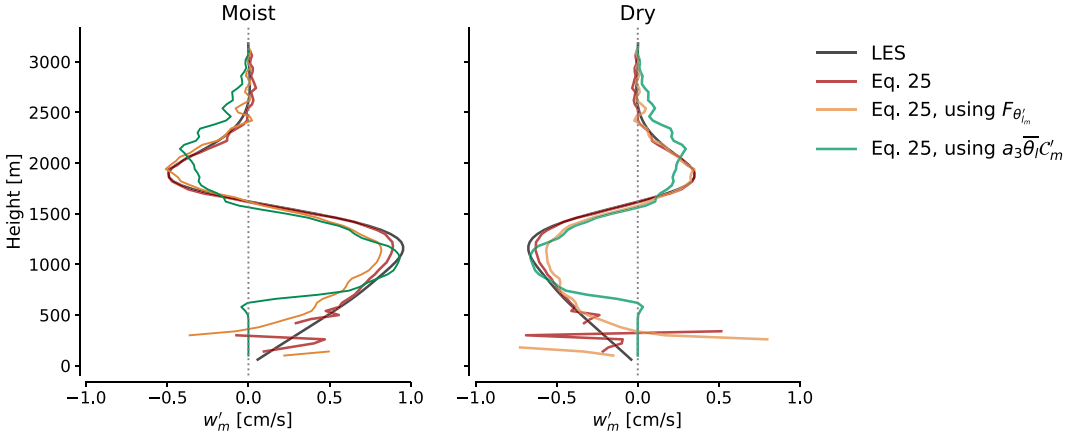

FIG. 12. w'_m derived directly from the LES model (black line) and modeled by Eq. (25) (maroon line), averaged over (left) moist and (right) dry regions and over 10–16 h. Note also the comparatively small error made if $F_{\theta'_{lv_m}}$ is used instead of $F_{\theta'_{lv_m}}$, or $a_3\overline{\theta_l}\mathcal{C}'_m$ is used instead of the convergence of $F_{\theta'_{lv_m}}$ in Eq. (25) (yellow and sea green lines).

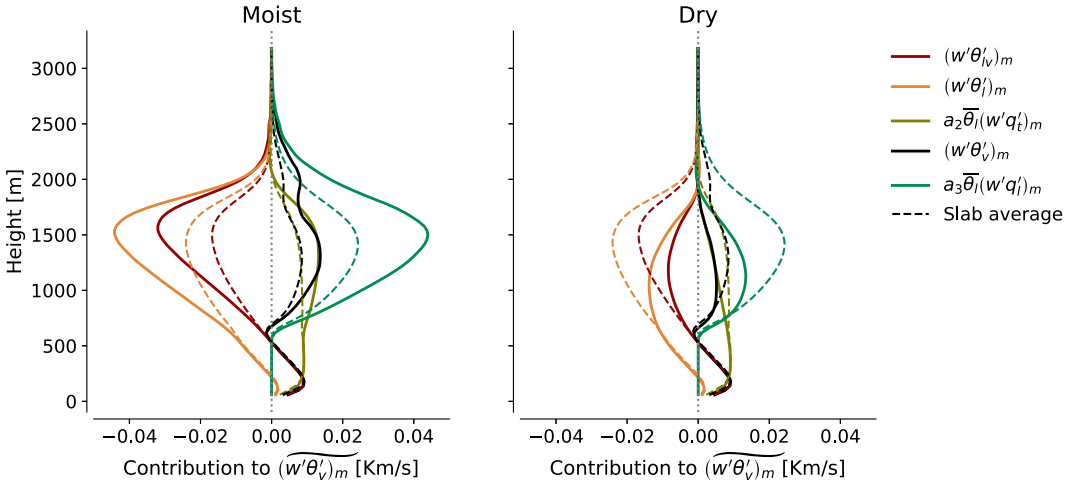

FIG. 13. Grid-resolved, vertical mesoscale-filtered fluxes $(w'\theta'_v)_m$ and $(w'\theta'_{lv})_m$ and their contributions from $(w'\theta'_l)_m$, $(w'q'_t)_m$, and $(w'q'_l)_m$ as defined in Eq. (14), averaged over (left) moist and (right) dry mesoscale regions (unbroken lines) and over the entire horizontal slab (dashed lines, copied from Fig. 2) over 10–16 h. The region-averaged flux anomaly $\widetilde{F_{\chi'_m}}$ [Eq. (19)] is the difference between the unbroken and dashed lines for each variable.

Hence, we have arrived at the heart of the mechanism: horizontal, mesoscale anomalies in the same vertical structure of the net condensation $\mathcal{C}$ that governs the slab-mean layer's evolution have, under WTG, as a consequence that they develop mesoscale vertical motion of a few centimeters per second. To demonstrate this explicitly, w'_m remains accurately predicted even when substituting $a_3\overline{\theta}_l\mathcal{C}'_m$ for the convergence of $F_{\theta'_{lv_m}}$ in Eq. (25) (green lines in Fig. 12).

Note that if we proceed along similar lines as above using Betts's (1973) original view of the slab-averaged problem, i.e., using mesoscale anomalies in $w'\theta'_l$ instead of $w'\theta'_{lv}$ to explain w'_m, the analysis remains largely unchanged, because, following the discussion in section 3, $w'\theta'_l$ too is well-known to be chiefly governed by $\mathcal{C}$. Since this view ignores virtual effects on the evolution of θ'_{v_m} [see Eq. (21)], it is slightly less accurate, but remains adequate for predicting w'_m (yellow lines in Fig. 12). We emphasize that also in this view, w'_m remains rooted in net condensation.

4) BB17's MODEL

To complete the argument, one may multiply Eq. (25) with the negative, mean moisture gradient to finally arrive at a model for the onset of q'_{t_m}, formulated in terms of anomalous heat fluxes and the ratio of mean flow gradients,

$$\frac{\partial q'_{t_m}}{\partial t} \sim -w'_m\Gamma_{q_t} \approx \frac{1}{\rho_0}\frac{\partial}{\partial z}(\rho_0 F_{\theta'_{lv_m}})\frac{\Gamma_{q_t}}{\Gamma_{\theta_{lv}}}, \tag{26}$$

which Fig. 14 shows is also accurate, and mostly captured even when replacing $F_{\theta'_{lv_m}}$ by $F_{\theta'_{l_m}}$ or its divergence by $-a_3\overline{\theta}_l\mathcal{C}'_m$.

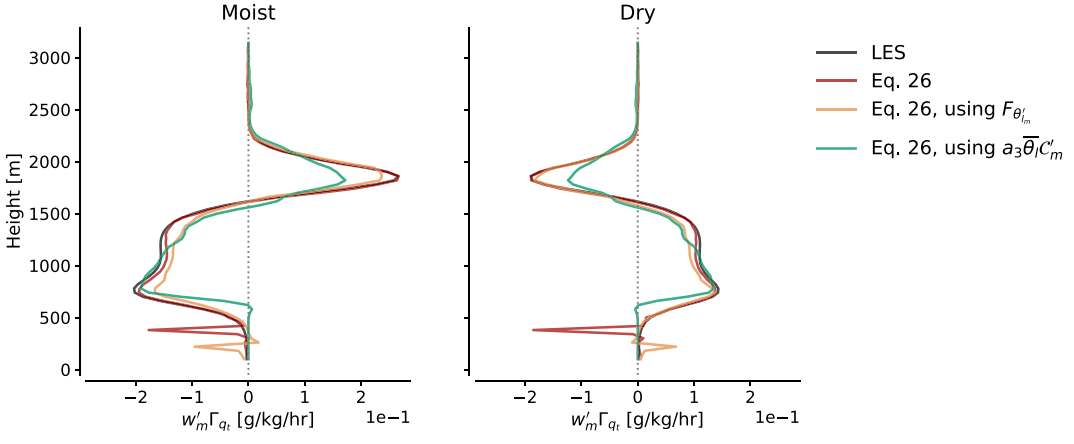

FIG. 14. $w'_m\Gamma_{q_t}$ derived directly from the LES model (black line) and following Eq. (26) (maroon line), averaged over (left) moist and (right) dry regions and over 10–16 h. Also shown are results if $F_{\theta'_{l_m}}$ is used instead of $F_{\theta'_{lv_m}}$, or $a_3\overline{\theta}_l\mathcal{C}'_m$ is used instead of the divergence of $F_{\theta'_{lv_m}}$ in Eq. (26) (yellow and sea green lines).

Equation (26) is a succinct summary of the model presented by BB17, combining the significant terms in their Eqs. (20) and (32).

5. Bulk model for the instability

As BB17 note, the vertical integral of Eq. (26) can be understood as negative gross moist stability of moisture fluctuations, as often used in models of deep convection (Neelin and Held 1987; Raymond et al. 2009). But because of the absence of horizontal heterogeneity in radiation and precipitation in our simulations, we can here simplify the instability a little further than studies of deep convection typically do. In particular, we will close a simple, linear bulk instability model for the development of the moisture fluctuations, and examine the conditions of this model in some detail.

a. Linear instability model

To close a positive feedback loop driving the development of q'_{t_m}, such fluctuations must lead directly to $F_{\theta'_{lv_m}}$, because vertical gradients in $F_{\theta'_{lv_m}}$ lead to mesoscale moistening anomalies following Eq. (26). Since $\mathcal{C}'_m$ supports $F_{\theta'_{lv_m}}$ [Eq. (23) and Fig. 13], an intuitive basis for this closure is to assume that a moister cloud layer is all that is needed for cumuli growing into it to condense more water vapor. Figure 6 confirms that cloud-layer q'_{t_m} and $\mathcal{C}'_m$ are well collocated. BB17 sketch a similar picture. However, a mathematical, theoretically founded description of the closure is still missing. Therefore, we suggest one here.

Our model will describe the time evolution of bulk mesoscale moisture fluctuations, $\langle q'_{t_m} \rangle$. Vertical, partial integration of Eq. (26) using Eq. (17) gives

$$\frac{\partial \langle q'_{t_m} \rangle}{\partial t} \approx -\frac{\rho_0}{\int_0^{z_\infty} \rho_0 dz} F_{\theta'_{lv_m}} \frac{\Gamma_{q_t}}{\Gamma_{\theta_{lv}}}\bigg|_0^{z_\infty} - \left\langle F_{\theta'_{lv_m}} \frac{\partial}{\partial z}\left(\frac{\Gamma_{q_t}}{\Gamma_{\theta_{lv}}}\right)\right\rangle. \tag{27}$$

Note that $F_{\theta'_{lv_m}} = 0$ above the cloud layer and at the surface, courtesy of our lower boundary condition, setting the first term to zero. If we additionally assume that $(\partial/\partial z)(\Gamma_{q_t}/\Gamma_{\theta_{lv}})$ is approximately constant with height, we may move it outside the integral:

$$\frac{\partial \langle q'_{t_m} \rangle}{\partial t} \approx -\frac{\partial}{\partial z}\left(\frac{\Gamma_{q_t}}{\Gamma_{\theta_{lv}}}\right)\left\langle F_{\theta'_{lv_m}} \right\rangle. \tag{28}$$

As we will discuss in a moment, this assumption is not entirely accurate, but sufficiently reasonable through the cloud layer (not shown) that it is worth making in the interest of showing that bulk moistening of moist, mesoscale regions is governed by the integrated heat flux anomaly. Any parameterization that relates such heat fluxes to q'_{t_m} suffices to close the model, and many such parameterizations can be imagined. In the spirit of Betts (1975), we will merely use a simplified mass-flux approximation:

$$F_{\theta'_{lv_m}} \approx -a_3 \overline{\theta_l} F_{q'_{t_m}} \tag{29a}$$

$$\approx -k_1 a_3 \overline{\theta_l} w^* q'_{l_m} \tag{29b}$$

$$\approx -k \overline{\theta_l} w^* q'_{t_m}. \tag{29c}$$

To write Eq. (29b), we take w^* to be a characteristic vertical velocity, obtained by averaging w over all cloudy cells in our simulation, ignore entrainment and detrainment effects, and do not use cloud core variables, which would give more accurate results (Siebesma and Cuijpers 1995). However, proceeding in this manner lets us relate mesoscale fluctuations in in-cloud liquid water directly to q'_{l_m} only. Since these assumptions yield errors only in the flux anomaly's magnitude, but not in the shape of its vertical profile (Siebesma and Cuijpers 1995), we correct them with a second constant k_1. To write Eq. (29c), we also assume $q'_{l_m} \propto q'_{t_m}$, and that equality can be restored by a single model constant k which subsumes k_1 and a_3. This amounts to assuming that mesoscale fluctuations in the saturation specific humidity are small.

In spite of all these assumptions, we consider Eq. (29c) with $k = 0.3$ adequate for the present discussion, cf. Fig. 15a. Inserting this relation in Eq. (28) allows framing the growth of column-averaged mesoscale moisture fluctuations as a linear instability problem, whose time scale is $\tau_{q'_{t_m}}$:

$$\frac{\partial \langle q'_{t_m} \rangle}{\partial t} \approx \frac{\langle q'_{t_m} \rangle}{\tau_{q'_{t_m}}}, \tag{30a}$$

$$\tau_{q'_{t_m}} = \frac{1}{k \overline{\theta_l} w^* \dfrac{\partial}{\partial z}\left(\dfrac{\Gamma_{q_t}}{\Gamma_{\theta_{lv}}}\right)}. \tag{30b}$$

Equation (30) remains rather accurate (Fig. 15b), diagnosing a time scale for the instability of almost 4 h in our simulation. The model is also plotted in Fig. 8.

While illustrative, it is prudent to ask if Eq. (29), upon which this time scale estimate rests, is reliable. Since it depends heavily on w^*, which is not well-constrained by any argument we have made, but is energetically supported by in-cloud turbulence at the very smallest scales our numerical model resolves, this is in fact quite questionable. BB17, who estimate the time scale without reference to a model for it, obtain a significantly larger number (15 h) than we do, suggesting that the mechanism may exhibit a strong numerical dependence, as is observed for models of self-aggregating deep convection (e.g., Muller and Held 2012; Wing et al. 2020). We devote a separate manuscript to this issue (Janssens et al. 2023).

b. Condition for instability

If the assumptions made in deriving Eq. (30) are generally valid, its only condition for $\langle q'_{t_m} \rangle$ growth is that the vertically averaged $(\partial/\partial_z)(\Gamma_{q_t}/\Gamma_{\theta_{lv}}) > 0$. This requirement arises because the divergence of $F_{\theta'_{lv_m}}$ itself integrates to zero when the surface fluxes are horizontally homogeneous. Were there a linear, mixing-line relation between $\overline{\theta_{lv}}$ and $\overline{q_t}$ throughout the boundary layer, $\Gamma_{q_t} \propto \Gamma_{\theta_{lv}}$ and any moisture convergence due to anomalous cloud-layer condensation would be exactly offset by inversion-layer moisture divergence due to anomalous evaporation: Eq. (26) would integrate to zero. BB17 arrive at a similar condition, but formulate it as a demand that a convex relation must exist between $\overline{q_t}(z)$ and $\overline{\theta_{lv}}(z)$ (or another

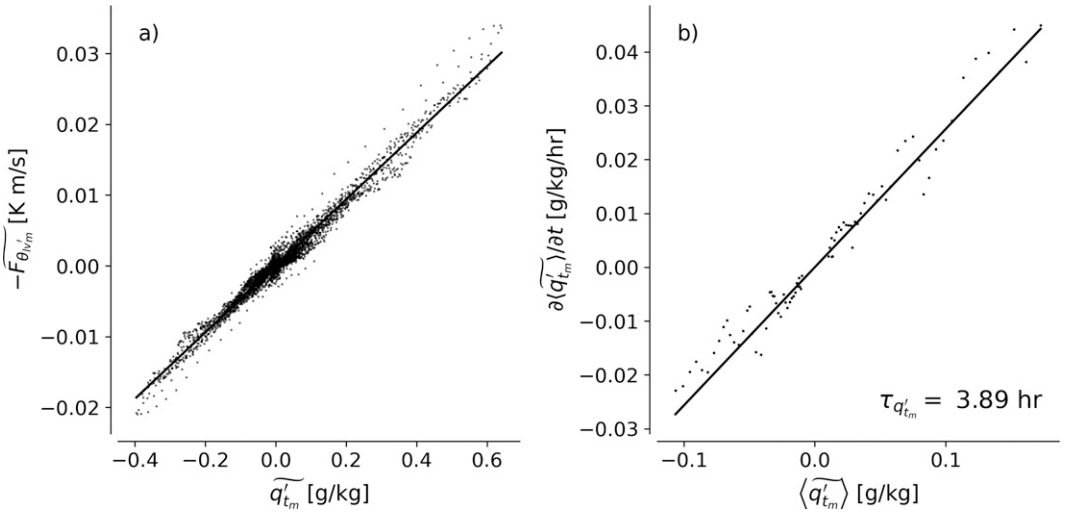

FIG. 15. Scatter plots of moist- and dry-region-averaged (a) q'_{t_m} against $-F_{\theta'_{lv_m}}$ and (b) $\langle q'_{t_m}\rangle$ against $\langle\partial q'_{t_m}\rangle/\partial t$, for all fields between 6 and 16 h (dots). Lines follow (a) Eq. (29), with constants $w^* = 0.52\,\mathrm{m\,s^{-1}}$ and $k = 0.3$ and (b) Eq. (30a), with $(\partial/\partial z)(\Gamma_{q_t}/\Gamma_{\theta v}) = 1.5\times10^{-3}\,\mathrm{g\,kg^{-1}\,K^{-1}\,m^{-1}}$. The constants are derived from the LES as described in the text. The time scale implied by the line in (b) [Eq. (30b)] is annotated.

pair of conserved thermodynamic variables).[1] For profiles without discontinuities, this follows from rewriting

$$\frac{\partial}{\partial z}\left(\frac{\Gamma_{q_t}}{\Gamma_{\theta_{lv}}}\right) = \Gamma_{\theta_{lv}}\frac{\partial^2\overline{q_t}}{\partial\overline{\theta_{lv}}^2} \tag{31}$$

with the quotient rule of calculus. Considering the most general case, where the term is kept under the integral [Eq. (27)], it is clear that a stable stratification ($\Gamma_{\theta_{lv}} > 0$) and $\partial^2\overline{q_t}/\partial\overline{\theta_{lv}}^2 > 0$ are needed to locally scale $F_{\theta'_{lv_m}} < 0$ into positive gradient production of q'_{t_m}. In fact, since $F_{\theta'_{lv_m}} < 0$ *throughout* the moist cloud layer, all that is required for the growth of $\langle q'_{t_m}\rangle$ is that the cloud-layer-*average* $\partial^2\overline{q_t}/\partial\overline{\theta_{lv}}^2 > 0$.

While Fig. 15 indicates that assuming such a cloud-layer average $\partial^2\overline{q_t}/\partial\overline{\theta_{lv}}^2$ suffices to accurately pose Eq. (30), Fig. 16 indicates that after 16 h of simulation, the curvature really stems from two distinct, convex regions (thick lines in Fig. 16a), resulting in two distinct lobes that make the integral Eq. (27) positive (Fig. 16b). The first convex region resides between the upper cloud layer and free troposphere. It emerges from the piecewise linear initial state (gray line in Fig. 16a), which anticipates the formation of the trade inversion. This state curves into a strictly convex feature once the discontinuity is broken. Its product with the large, local $F_{\theta'_{lv_m}}$ gives the upper lobe in Fig. 16b. The second convex region resides in the lower cloud layer. It has developed spontaneously from the initial condition, which *did* lie on a local mixing line and therefore inhibited local contributions toward the scale growth. However, after 16 h, a region of large $(\partial/\partial_z)(\Gamma_{q_t}/\Gamma_{\theta_{lv}}) > 0$ has developed, which, in spite of scaling a locally small $F_{\theta'_{lv_m}}$, results in a substantial lower lobe in Fig. 16b. Each lobe contributes roughly half the moisture convergence into the moist region.

Which process is responsible for drawing the mean thermodynamic state away from a mixing line, and for developing these convex features? BB17 emphasize the importance of large-scale, radiative cooling or cold-air advection (their Fig. 15). These processes are essential for creating the instabilities that lead to turbulence and cumulus convection. However, focusing on them draws one's attention away from the fact that it is the vertical inhomogeneity in the convective adjustment to these forcings that creates the internal, convex layers in Fig. 16. Focusing for a moment on the contributions to the lower cloud-layer tendency in Fig. 16, one may recognize that the large-scale forcing is constant in height throughout the convex layer: in our simulation setup, it could only ever translate the initial mixing line horizontally, and not pull it into the curved shape it attains. Instead, curvature is generated by the vertical flux convergence terms in Eq. (4), which respond to the constant forcing by heating and moistening the cloud layer in vertically varying fashion. A similar story holds in the inversion, where flux convergence generates convexity through cooling and moistening.

To understand how vertical fluxes underpin convexity generation in these two layers, consider Fig. 17, which plots $\overline{\theta_{lv}}$ and $\overline{q_t}$ and their vertical flux convergence as a function of height. In the inversion, these flux convergences are energetically rooted in net evaporation (Fig. 1, repeated here as Fig. 17e), which transitions from zero at inversion base to an evaporation peak and back to zero in the free troposphere. These transitions occur both smoothly and over a finite height, endowing curvature to the liquid water, heat, and moisture flux convergence profiles over a broad region. In turn, the smooth, broad evaporation peak in the trade wind inversion layer arises from a population of individual,

[1] BB17 call this relationship "concave," but since the curve in question has a positive second derivative, we will adopt the more usual mathematical term for such relations, "convex," here.

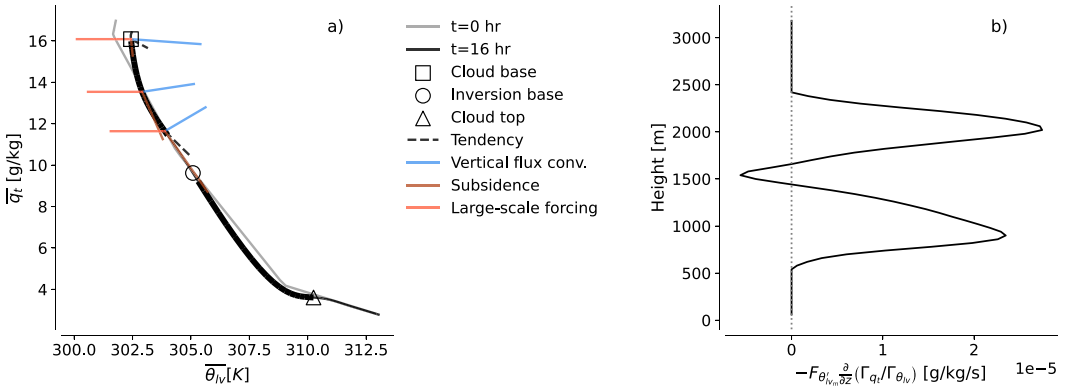

FIG. 16. (a) Relationship between $\overline{\theta_{lv}}$ and $\overline{q_t}$ in the initial state (gray line) and after 16 h (black line). At 16 h, the variables are convexly related in the lower and upper cloud layers, indicated by thick black lines. Vectors indicating budget contributions to Eq. (4) are drawn at several altitudes in the lower, convex layer. The circle indicates the inversion base, the square the cloud base, and the triangle the cloud top. (b) Moist-region-averaged heightwise contributions toward the vertical integral Eq. (27).

intermittent cloud turrets, each of which evaporates at a slightly different height. This is evidenced by the broad, upper peak in the cloud-top height distribution around 1750 m in Fig. 17f, which spans the inversion layer and matches both the evaporation and flux convergence peaks. When working against the lapse rates of our free troposphere, the evaporation moistens the inversion more efficiently than cooling it, compared to how condensation moistened and heated the cloud layer; this is what finally renders $\partial^2\overline{q_t}/\partial\overline{\theta_{lv}}^2 > 0$.

A similar explanation for the curvature developing in the lower cloud layer is offered by Albright et al. (2022, manuscript submitted to *J. Atmos. Sci.*). In observations, the cloud-top height distribution features a second mode due to very shallow cumuli between 500 and 1000 m. Our simulation exhibits the same bimodality (Fig. 17f). The shallow mode spans the so-called transition layer, which observations both old (Augstein et al. 1973) and very recent (Albright et al. 2022) indicate is usually thick and curved—exactly as it is in Fig. 16. Albright et al. (2022, manuscript submitted to *J. Atmos. Sci.*) suggest that this structure may be brought about by the population of very shallow clouds that inhabit the layer: at cloud base, the shallow clouds warm and moisten in accordance with their deeper counterparts. Yet they quickly evaporate, leading to the rapid drop in condensation above 700 m in Fig. 17e. Analogous to how deeper clouds cool and moisten the inversion, the evaporation of the shallow cloud population, exhibited by the lower peak of the cloud-top-height distribution in Fig. 17f, yields the cooling and moistening features in the lower cloud layer observed in Figs. 17b and 17d. Once all the very shallow clouds have dissipated, the positive net condensation in the remaining, deeper clouds returns to heating and moistening the layer until the inversion base. The result is a transition layer characterized by curved flux convergences of heat and moisture, which translate into curved profiles of $\overline{\theta_{lv}}$ and $\overline{q_t}$ (corresponding arrows in Figs. 17a–d). As visualized in Fig. 16a, both fluxes contribute to make $\partial^2\overline{q_t}/\partial\overline{\theta_{lv}}^2 > 0$.

Let us finally formalize the observations made above somewhat, by analyzing what is mathematically demanded from flux convergences of moisture and heat to bring about $\partial^2\overline{q_t}/\partial\overline{\theta_{lv}}^2 > 0$

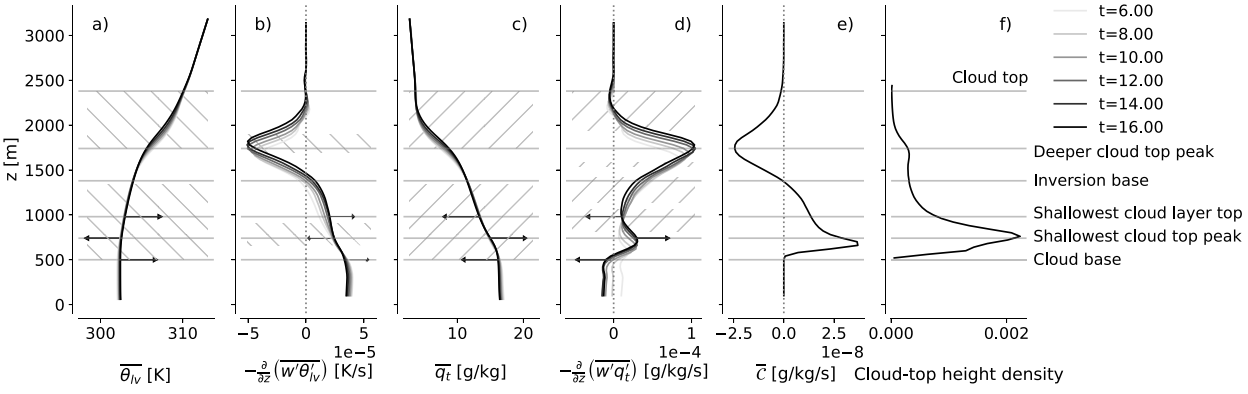

FIG. 17. Time evolution of vertical profiles of (a) $\overline{\theta_{lv}}$, (b) $-(\partial/\partial z)(\overline{w'\theta'_{lv}})$, (c) $\overline{q_t}$, (d) $-(\partial/\partial z)(\overline{w'q'_t})$, (e) $\overline{C}$, and (f) vertical distribution of cloud-top height throughout the simulation. Hatches indicate areas where (a),(c) $\partial^2\overline{q_t}/\partial\overline{\theta_{lv}}^2 > 0$, (b) $\partial^3\overline{w'\theta'_{lv}}/\partial z^3 < 0$, and (c) $\partial^3\overline{w'q'_t}/\partial z^3 < 0$ at $t = 16$ h. Arrows emphasize the action of condensation and evaporation in very shallow clouds over the transition layer on the flux convergence terms and on the thermodynamic variables.

from situations where $\overline{q_t}$ and $\overline{\theta_{lv}}$ are initially at most linear functions of height, where $\Gamma_{\theta_{lv}} > 0$ and where $\Gamma_{q_t} < 0$. By deriving an evolution equation for $\partial^2\overline{q_t}/\partial\overline{\theta_{lv}}^2 > 0$ (see appendix B), such a requirement reads

$$\frac{1}{\rho_0}\frac{\partial^3}{\partial z^3}(\rho_0\overline{w'q_t'}) < 0, \tag{32a}$$

$$\frac{1}{\rho_0}\frac{\partial^3}{\partial z^3}(\rho_0\overline{w'\theta_{lv}'}) < 0. \tag{32b}$$

Regions where these conditions are satisfied are hatched in Figs. 17b and 17d; they also overlap regions where the mean state becomes convex in our simulation. The derivation of this condition is not strictly valid for our simulation's inversion layer, as its *piecewise* linear initial condition (i) cannot be differentiated over the discontinuity, and (ii) already implied a convex relation between the cloud and inversion layers. However, LES under vertically constant forcings launched from continuous, quasi-linear initial conditions *do* spontaneously develop transition and inversion layers with the same convex vertical structure that would result from Eq. (32), e.g., the idealized framework developed by Bellon and Stevens (2012), later used for studies of cloud organization by Vogel et al. (2016). In fact, the structures are evident in many other LESs that exhibit length scale growth in their cumulus fields, such as the original Rain in Cumulus over Ocean (RICO) ensemble (van Zanten et al. 2011) and its derivatives (e.g., Seifert et al. 2015; Anurose et al. 2020), the simulations of length scale growth presented by Narenpitak et al. (2021) and even the simulations (Blossey et al. 2013) that BB17 develop their theory upon. The condition Eq. (32a) is satisfied even for the moist static energy fluxes diagnosed over the undisturbed BOMEX period by Nitta and Esbensen (1974); their satellite images also indicate that large cloud structures developed even during the undisturbed period so long associated only with small, stable cumuli.

Taken together, this set of evidence gives us confidence that the satisfaction of the convexity condition required to destabilize mesoscale moisture fluctuations is inherent to slab-averaged cumulus convection: it develops from the vertical inhomogeneity of condensation and mixing in cumulus clouds in response to forcings such as boundary layer–averaged radiative cooling and surface temperatures, under the lapse rates of heat and moisture that characterize the trades. Hence, as long as the larger-scale and boundary forcing support turbulent fluxes that maintain a cumulus-topped boundary layer, length scale growth in moisture fluctuations will be an intrinsic feature of the resulting convection.

6. Discussion and outlook

Before summarizing, let us review three consequences of this rather striking conclusion.

a. *Relevance of circulation-driven scale growth*

To what extent does condensation-driven scale growth matter in nature? To lay bare the essence of the mechanism, we have here made a number of simplifications that are probably too restrictive for us to speak authoritatively on this matter. In particular, our assumptions that (i) the surface fluxes and large-scale advection of heat and moisture are fixed in space and time, (ii) precipitation and interactive radiation do not play a role, and (iii) the mean environment is rather stationary imply that we ignore several important processes that in nature will modulate the instability we discuss. Since the relative effects of such processes in patterning the trades is a topic of active research, we briefly discuss some anticipated consequences of these assumptions here.

First, if q_{t_m}' reach the surface, Eq. (27) shows that surface flux anomalies could potentially oppose further moistening. At constant sea surface temperatures and with mild precipitation, BB17 show such effects to be of second-order importance, indicating that the well-mixed layer may remain quasi stationary and tied to the local surface conditions at large spatial scales, as is often assumed in models of deep convective self-organization (e.g., Emanuel et al. 2014). This matters, since sea surface temperature influences the vigor of the convection (measured here through w^*) and thus, through Eq. (30), can explain, e.g., the more rapid production of mesoscale circulations and moist patches over a warmer ocean simulated by Vogel et al. (2016). Extensions to also study sea surface temperature heterogeneity, which amplifies circulations (Park et al. 2006), are easily imagined.

Heterogeneous radiation can support shallow circulations in detailed (Klinger et al. 2017) and conceptual (Naumann et al. 2019) simulations of cumulus-topped boundary layers. In particular, when the circulations are sufficiently strong to begin detraining significant amounts of inversion cloud atop the moist region's boundary layer, they reinforce the anomalous heating that here drives the circulations (BB17; Vogel et al. 2020b); these effects would accelerate the mechanism beyond the time scale derived in Eq. (30b).

If the shallow cumulus layer deepens sufficiently for precipitation to form, we must further amend our estimates. Slab-averaged precipitation will on one hand reinforce $\Gamma_{q_t} < 0$ in the cloud layer, but on the other reduce the inversion-layer evaporation upon which $F_{\theta_{lv}}$ relies (Albrecht 1993); the relative effects of these factors seem to enhance length scale growth in the simulations conducted by BB17. However, precipitation that is sufficiently vigorous to produce cold pools will locally discourage the formation of convection upon which our simulated circulations rely, and may thus relieve gradient production driven by cloudy updrafts as the leading-order process governing the spatial distribution of moisture and clouds; such transitions seem to take place in mesoscale LES of RICO (Seifert and Heus 2013; Seifert et al. 2015; Anurose et al. 2020; Thomas et al. 2021). When cold pools dominate, their length scale replaces that of the clouds as the descriptor of the mesoscales (Matheou and Lamaakel 2021), and the length scales of cloud-free areas emerge as the natural complement to those of the clouds themselves as measures of the resulting cloud organization (Janssens et al. 2021; Schulz et al. 2021). However, a broad regime of conditions can be imagined where both circulations and cold pools act in concert to form or maintain convection patterns, e.g., under strong inversions and high surface fluxes, as for the patterns labeled "flowers" and "fish" in Schulz et al. (2021), or through an imposed large-scale ascent which may vary from being upward and

later downward (Narenpitak et al. 2021). Such situations deserve more study.

Finally, we note that recent observations (George et al. 2021, 2022) suggest that mesoscale circulations with a similar magnitude and vertical structure as we find in our simulations pervade the trades. Also, any process which gives rise to mesoscale circulations will be amplified by the mechanism discussed here. Hence, while more research is needed to explicitly root these observations in the dynamics described here and by BB17, the mechanism warrants consideration in further studies attempting to explain mesoscale variability in clouds and moisture.

b. *Connection to trade-inversion growth*

Application of the WTG approximation implies that the level of the trade inversion is rather constant over our domain, in spite of large moisture fluctuations accumulating over the layer. The level of this trade inversion is governed by $w'\theta'_{lv}$ (section 3; Stevens 2007), while fluctuations in $w'\theta'_{lv}$ govern scale growth.

Combining these observations highlights a practical way in which mesoscale cloud fluctuations affect the slab-averaged layer: since $\overline{w'\theta'_{lv}}$ skews toward the profiles set by the deeper clouds in moist regions (see Fig. 13), scale growth accelerates growth of the inversion beyond the rates we find in simulations on smaller domains (10 km $\times$ 10 km, not shown).

The upshot is that scale growth may influence transitions to deep convection. In fact, after around 20 h, the moist patches in our simulation develop deep, organized clouds, aided by the lack of subsidence above 2 km in our simulation setup. This feedback is similar to that observed by Vogel et al. (2016) for initially shallow, nonprecipitating convection. Hence, the unstable nature of shallow convection to scale growth may give it a role to play in explaining the initiation of organized, deep convection too.

c. *Connection to cloud feedback estimates*

How does the scale growth mechanism affect cloud fraction, which to first order governs the trades' contribution to the equilibrium climate sensitivity, and which remains poorly constrained in general circulation models (Zelinka et al. 2020)? Figure 4 shows the cloud fraction is remarkably robust over our 16 h of simulation, as cloudiness increases in moist regions compensate reductions in dry regions. The small, observed reduction can be attributed to the developing circulation's tendency to contract the moist regions at the expense of the dry regions (Fig. 8), an observation which is consistent with, e.g., Vogel et al. (2016). Even if the mechanism would strengthen above warmer sea surfaces, in more weakly subsiding environments and weaker mean gradients, it would thus likely support the emerging picture that trade wind cloudiness is rather insensitive to changes in the overall climate (Myers et al. 2021; Cesana and Del Genio 2021).

However, two notes on this statement motivate further research. First, the cloud fraction will be sensitive to the developing inversion-layer outflows' ability to sustain extensive sheets of inversion cloud, which does not occur in our simulations, but is observed in other studies (BB17; Vogel et al. 2020b; Narenpitak et al. 2021; Bony et al. 2020). Many situations can be imagined to feature higher inversion cloud fractions than BOMEX, whose inversion is rather dry and warm. More systematic study of the mechanism over different environmental conditions using more realistic physics than we do here is warranted.

This is particularly pertinent because approaches such as those taken by Myers et al. (2021) and Cesana and Del Genio (2021) essentially assume large-scale cloud-controlling variables set the cloud fraction. Recent observations seem to dovetail with this approach, suggesting that (presumably externally induced) variability in mesoscale vertical velocity directly controls cloud-base mass fluxes and cloud fractions (Bony and Stevens 2019; Vogel et al. 2020a; George et al. 2021).

Our results, however, suggest the opposite view: here, spatial variability in the convective mass flux, filtered and averaged over mesoscale moist and dry regions, controls variability in mesoscale vertical velocity. The role of the resulting circulation is simply to set the right cloud-layer thermodynamic environment for subsequent clouds to preferentially form in, and this is what ultimately controls the cloudiness. If the view suggested by our simulations turns out to matter in nature, questions arise regarding the validity of approaches such as those taken by Myers et al. (2021); Cesana and Del Genio (2021), because they ignore that shallow convective clouds may simply control their own cloud-controlling variables. Reconciling the views put forward on the basis of recent observations with ours is thus a recommendation with substantial ramifications (Bony et al. 2015). Fortunately, the data from the recent EUREC^{4}A field campaign (Bony et al. 2017; Stevens et al. 2021) may be sufficiently detailed to begin answering such questions, boding well of our understanding of the significance of self-organizing shallow cloud patterns to climate.

7. Summary and concluding remarks

Building on BB17, we have formulated an idealized model for a linear instability that leads to uninhibited length scale growth of moisture fluctuations in layers of nonprecipitating trade wind cumulus [Eq. (30)]. Using only well-established theory and a classical large-eddy simulation setup (Siebesma et al. 2003) with no heterogeneous surface forcing, radiation or precipitation, the model explains how small spatial differences in the amount of condensation in shallow cumulus clouds produce a mesoscale circulation under the assumption of weak, horizontal mesoscale temperature gradients. The circulation converges moisture into regions that consequently support more cumulus clouds, diabatic heating, and a stronger circulation; these regions grow exponentially in intensity and scale (Fig. 8) until they are modulated by an outer length scale (here the finite size of our LES domains) or translate the problem to a regime of different leading-order dynamics, e.g., driven by precipitation or radiation, which we do not simulate.

We further clarify that the imposed, larger-scale environment is only required to support a slab-averaged cumulus layer. If it does so, the moisture instability is free to develop on top of the mean state as a function only of turbulent fluxes of heat and moisture [Eq. (32)] because cumulus convection naturally adjusts inhomogeneously to vertically homogeneous forcing, giving rise to the internal transition and inversion layers. This property gives rise to the right curvatures in the mean state for mesoscale condensation anomalies to accumulate mesoscale moisture fluctuations.

In all, we conclude that shallow convection is therefore intrinsically unstable to scale growth, a result which is implied even by the results reported by Nitta and Esbensen (1974) for the "undisturbed" BOMEX period, upon which many theories that assume horizontal homogeneity in nonprecipitating trade wind cloudiness rely. It is high time to move beyond such ideas.

As a final remark, we note how striking it is that we have only required well-established, classical theory for our discussion. As noted at the outset, the structure of the mean trades was elucidated 60 years ago. WTG's utility has been known to some for almost 40 years (Held and Hoskins 1985). The interpretation of the instability we have discussed as negative values in moist gross stability relates to classical, influential concepts from tropical meteorology (Neelin and Held 1987). One may even argue that the instability we describe is fundamentally nothing but convective instability of the second kind (CISK; Charney and Eliassen 1964), perhaps finally finding a subtropical home for this highly scrutinized and criticized idea.

This motivates us to conclude simply by asking, What else might we learn from the insights of the giants of tropical meteorology when exploring the still rather uncharted territory of shallow convection in the mesoscale trades?

Acknowledgments. The authors wish to acknowledge Thomas Frederikse and Harm Jonker, whose unpublished work stimulated our initial inquiries into scale growth in cumulus layers. MJ warmly acknowledges conversations with Anna Lea Albright on the role of very shallow cumulus in shaping the transition layer. CvH acknowledges funding from the Dutch Research Council (NWO) (Grant: VI.Vidi.192.068). A. Pier Siebesma acknowledges funding by the European Union's Horizon 2020 research and innovation program under Grant Agreement 820829 (CONSTRAIN project). FG acknowledges support from the Branco Weiss Fellowship—Society in Science, administered by ETH Zürich, and from an NWO Veni grant. We thank the NWO for use of its computer facilities (Project 2021/ENW/01081379). Finally, we are grateful to three anonymous reviewers, who have improved the quality and clarity of this manuscript. Especially the framing of the ideas expressed in section 5b rely heavily on their remarks.

Data availability statement. The version of DALES (https://doi.org/10.5281/zenodo.6545655), the numerical settings (https://doi.org/10.6084/m9.figshare.19762219.v1), and routines used to generate the plots presented herein (https://doi.org/10.5281/zenodo.6545916) are publicly available. Living repositories for DALES and the postprocessing scripts are available at https://github.com/dalesteam/dales and https://github.com/martinjanssens/ppagg.

APPENDIX A

Budgets of Scalars

a. Derivation of Eq. (3)

Equation (3) in the main text may be derived from Eq. (1) by making use of the decomposition into slab-averaged (overbars) and fluctuating (primes) quantities [Eq. (2)], yielding the following expansions for the horizontal and vertical advection terms:

$$\frac{\partial}{\partial x_{\mathrm{jh}}}(u_{\mathrm{jh}}\chi) = \frac{\partial}{\partial x_{\mathrm{jh}}}(\overline{u_{\mathrm{jh}}}\chi + u'_{\mathrm{jh}}\overline{\chi} + u'_{\mathrm{jh}}\chi') \tag{A1a}$$

$$= \chi\frac{\partial \overline{u_{\mathrm{jh}}}}{\partial x_{\mathrm{jh}}} + \overline{\chi}\frac{\partial u'_{\mathrm{jh}}}{\partial x_{\mathrm{jh}}} + \overline{u_{\mathrm{jh}}}\frac{\partial \chi}{\partial x_{\mathrm{jh}}} + u'_{\mathrm{jh}}\frac{\partial \overline{\chi}}{\partial x_{\mathrm{jh}}} + \frac{\partial}{\partial x_{\mathrm{jh}}}(u'_{\mathrm{jh}}\chi'), \tag{A1b}$$

$$\frac{1}{\rho_0}\frac{\partial}{\partial z}(\rho_0 w\chi) = \frac{1}{\rho_0}\frac{\partial}{\partial z}[\rho_0(\overline{w}\chi + w'\overline{\chi} + w'\chi')] \tag{A1c}$$

$$= \chi\left(\frac{\partial \overline{w}}{\partial z} + \frac{1}{\rho_0}\frac{\partial \rho_0}{\partial z}\overline{w}\right) + \overline{\chi}\left(\frac{\partial w'}{\partial z} + \frac{1}{\rho_0}\frac{\partial \rho_0}{\partial z}w'\right) + \overline{w}\frac{\partial \chi}{\partial z} + w'\frac{\partial \overline{\chi}}{\partial z} + \frac{1}{\rho_0}\frac{\partial}{\partial z}(\rho_0 w'\chi'). \tag{A1d}$$

In the anelastic approximation, conservation of mass demands:

$$\frac{\partial u_{\mathrm{jh}}}{\partial x_{\mathrm{jh}}} + \frac{\partial w}{\partial z} + \frac{1}{\rho_0}\frac{\partial \rho_0}{\partial z}w = 0, \tag{A2}$$

with the last term required to conserve the reference mass (Lilly 1996); it holds for both fluctuations and in the slab average. Therefore, when adding the expansions Eqs. (A1b) and (A1d), the respective sum of the first terms and second terms in these equations (those scaled by χ and $\overline{\chi}$) are zero, resulting in Eq. (3) of the main text. Note that because we solve our equations on a doubly periodic domain, Eq. (A2) requires $\overline{w} = 0$. Its effects in Eq. (3) are therefore prescribed, by setting $\overline{w}$ and scaling it with the local vertical gradient of χ.

b. Derivation of Eq. (18) for mesoscale scalar fluctuations

The main text's Eq. (18) can be derived from Eqs. (3) and (4) by subtracting the latter from the former (retaining all terms), which gives

$$\frac{\partial \chi'}{\partial t} = -\overline{u_{\mathrm{jh}}}\frac{\partial \chi'}{\partial x_j} - u'_{\mathrm{jh}}\frac{\partial \overline{\chi}}{\partial x_{\mathrm{jh}}} - \frac{\partial}{\partial x_{\mathrm{jh}}}(u'_{\mathrm{jh}}\chi' - \overline{u'_{\mathrm{jh}}\chi'}) - \overline{w}\frac{\partial \chi'}{\partial z} - w'\frac{\partial \overline{\chi}}{\partial z} - \frac{1}{\rho_0}\frac{\partial}{\partial z}[\rho_0(w'\chi' - \overline{w'\chi'})] + S'_\chi. \tag{A3}$$

To derive Eq. (18) from Eq. (A3), we have made a number of assumptions. In our LES model, whose results we analyze, use of doubly periodic boundary conditions enforces the following conditions on the horizontal advection of fluctuations:

$$\overline{u_{\mathrm{jh}}}\frac{\partial \chi'}{\partial x_j} = \frac{\partial}{\partial x_{\mathrm{jh}}}(\overline{u_{\mathrm{jh}}}\chi'), \tag{A4a}$$

$$u'_{\mathrm{jh}}\frac{\partial \overline{\chi}}{\partial x_{\mathrm{jh}}} = 0, \tag{A4b}$$

$$\frac{\partial}{\partial x_{\mathrm{jh}}}(\overline{u'_{\mathrm{jh}}\chi'}) = 0. \tag{A4c}$$

Thus, unless their effects would be prescribed or parameterized, our model does not account for (i) the advection of scalar fluctuations into the analyzed domain with the mean wind [Eq. (A4a)], (ii) interactions between horizontal gradients in χ larger than the domain [Eq. (A4b)], or (iii) slab-averaged, horizontal eddy fluxes into the domain [Eq. (A4c)]. For our idealized analysis of the onset of scale growth from local processes, these assumptions seem reasonable, but probably become untenable for analyses of finite, real-world domains with open boundaries.

Furthermore, we have in our analysis neglected the explicit influence of unresolved-scales effects. These would enter the analysis through additional diffusion terms on the right-hand side of Eq. (1). We do not present them in our equations, but we do compute them and include them in the appropriate flux divergence terms in the budgets presented in the text. At the mesoscales, which are far removed from their action on the smallest, resolved scales, their direct effects are small. Nevertheless, their influence in setting the fluxes which drive the model is nontrivial, as we will show in future work.

Finally, we have in our nonprecipitating simulations with homogeneous radiation not imposed any sources, rendering $S_\chi = 0$. Making these assumptions and applying a mesoscale filter to the resulting equation results in Eq. (18), and ensures its consistency with our LES model.

c. Moist and dry region averaging

Equation (18) is formulated in an Eulerian manner. When averaging it over moist and dry regions, as done in the main text, we risk that our local budgets become dominated by mean-flow advection of the regions. Since we are more interested in the evolution of the regions themselves, we note that we can make use of Reynolds's transport theorem (here manipulated with the divergence theorem)

$$\widetilde{\frac{\partial \chi'_m}{\partial t}} = \frac{\partial \widetilde{\chi'_m}}{\partial t} - \frac{\partial}{\partial x_{\mathrm{jh}}}\widetilde{(\chi'_m u^b_{\mathrm{jh}})}, \tag{A5}$$

where the tilde represents the moist or dry region averaging operator and u^b_j is the horizontal velocity of the region's boundary. The first term on the right-hand side of Eq. (A5) captures the evolution of χ'_m averaged over the moist and dry regions, in which we are primarily interested, and which is plotted in Figs. 7 and 11. The second term accounts for the advection and net expansion of the regions with u^b_{jh}. By decomposing u^b_{jh} into its contributions from mean flow advection ($\overline{u}_{\mathrm{jh}}$) and net expansion ($u^e_{\mathrm{jh}}$)

$$u^b_{\mathrm{jh}} = \overline{u}_{\mathrm{jh}} + u^e_{\mathrm{jh}} \tag{A6}$$

and inserting this into the second term on the right-hand side of Eq. (A5), we recognize that we may cancel the mean-flow advection term that results with the mean-flow advection contribution to the third term on the right-hand side of Eq. (18), if it is expanded as follows and region averaged:

$$\frac{\partial}{\partial x_{\mathrm{jh}}}(u_{\mathrm{jh}}\chi')_m = \frac{\partial}{\partial x_{\mathrm{jh}}}(\overline{u}_{\mathrm{jh}}\chi'_m) + \frac{\partial}{\partial x_{\mathrm{jh}}}(u_{\mathrm{jh}}\chi')_m. \tag{A7}$$

These operations leave a residual when comparing the region-averaged budgets to the first term on the right-hand side of Eq. (A5), due to u^e_{jh}. This is the term we dub "net region expansion" in the main text. Since this residual also includes errors from numerical integration of simulation output and Reynolds averaging, it is the least well-constrained term in our budgets, but we find it plausible to attribute its main vertical structure to net expansion of the moist regions at the expense of dry regions.

APPENDIX B

Derivation of the Evolution Equation for $\partial/\partial z(\Gamma_{q_t}/\Gamma_{\theta_{lv}})$

To analyze the onset and evolution of mean-state convexity, i.e., $\partial^2\overline{q_t}/\partial\overline{\theta_{lv}}^2 > 0$, we use the equivalence indicated in Eq. (31) and write an evolution equation for $\partial/\partial z(\Gamma_{q_t}/\Gamma_{\theta_{lv}})$ by differentiating it to time and applying the quotient rule of calculus twice. This results in the following relation, where we have attempted to retain some brevity by writing (repeated) vertical derivatives as (repeated) subscripts z:

$$\begin{aligned}\frac{\partial}{\partial t}\left(\frac{\overline{q_t}_z}{\overline{\theta_{lv}}_z}\right)_z = {} & \frac{1}{\overline{\theta_{lv}}_z}\left(\frac{\partial \overline{q_t}}{\partial t}\right)_{zz} - \frac{\overline{\theta_{lv}}_{zz}}{\overline{\theta_{lv}}_z^2}\left(\frac{\partial \overline{q_t}}{\partial t}\right)_z - \frac{\overline{q_t}_z}{\overline{\theta_{lv}}_z^2}\left(\frac{\partial \overline{\theta_{lv}}}{\partial t}\right)_{zz} \\ & + \left(2\frac{\overline{q_t}_z\overline{\theta_{lv}}_{zz}}{\overline{\theta_{lv}}_z^3} - \frac{\overline{q_t}_{zz}}{\overline{\theta_{lv}}_z^2}\right)\left(\frac{\partial \overline{\theta_{lv}}}{\partial t}\right)_z.\end{aligned} \tag{B1}$$

To determine which processes influence the left-hand side of this equation, we may expand the tendencies that appear on its right-hand side into their budget contributions from Eq. (4). Applying the vertical derivatives results in Eq. (B2):

$$\begin{aligned}\frac{\partial}{\partial t}\left(\frac{\overline{q_t}_z}{\overline{\theta_{lv}}_z}\right)_z = {} & \frac{1}{\overline{\theta_{lv}}_z}\left[-(\overline{w_{ls}q_t}_z)_{zz} - \frac{1}{\rho_0}(\rho_0\overline{w'q'_t})_{zzz} + \overline{S_{q_t}}_{zz}\right] \\ & - \frac{\overline{\theta_{lv}}_{zz}}{\overline{\theta_{lv}}_z^2}\left[-(\overline{w_{ls}q_t}_z)_z - \frac{1}{\rho_0}(\rho_0\overline{w'q'_t})_{zz} + \overline{S_{q_t}}_z\right] \\ & - \frac{\overline{q_t}_z}{\overline{\theta_{lv}}_z^2}\left[-(\overline{w_{ls}\theta_{lv}}_z)_{zz} - \frac{1}{\rho_0}(\rho_0\overline{w'\theta'_{lv}})_{zzz} + \overline{S_{\theta_{lv}}}_{zz}\right] \\ & + \left(2\frac{\overline{q_t}_z\overline{\theta_{lv}}_{zz}}{\overline{\theta_{lv}}_z^3} - \frac{\overline{q_t}_{zz}}{\overline{\theta_{lv}}_z^2}\right) \\ & \times \left[-(\overline{w_{ls}\theta_{lv}}_z)_z - \frac{1}{\rho_0}(\rho_0\overline{w'\theta'_{lv}})_{zz} + \overline{S_{\theta_{lv}}}_z\right].\end{aligned} \tag{B2}$$

Equation (B2) highlights a few interesting requirements for the development of convexity in the mean state. First, it shows that in the limit of linear mean profiles ($\overline{\theta_{lv}}_{zz} = \overline{q_t}_{zz} = 0$), the second and fourth term in Eq. (B2) are zero, constraining the responsibility for the onset of convexity development to processes that have curvature in their mean profiles (those in terms 1 and 3). In simulations where the subsidence and large-scale forcing profiles are initially at most *linear* functions of height, the only nonzero terms that remain in Eq. (B2) are third derivatives of the slab-mean fluxes. In fact, for $\Gamma_{\theta_{lv}} > 0$ and $\Gamma_{q_t} < 0$, these third derivatives must be negative to

initiate the development of convexity, i.e., $\partial/\partial t(\overline{q_t}_z/\overline{\theta_{lv}}_z)_z > 0$. The result is the condition Eq. (32) in the main text.

If $\overline{\theta_{lv}}$ and $\overline{q_t}$ have curvature in their profiles, the second and fourth terms are no longer necessarily zero, such that linear variations in subsidence and large-scale forcing, as well as curvature in the flux profiles, may have an effect.

REFERENCES

Agee, E. M., T. S. Chen, and K. E. Dowell, 1973: A review of mesoscale cellular convection. *Bull. Amer. Meteor. Soc.*, **54**, 1004–1012, https://doi.org/10.1175/1520-0477(1973)054<1004:AROMCC>2.0.CO;2.

Ahmed, F., and J. D. Neelin, 2019: Explaining scales and statistics of tropical precipitation clusters with a stochastic model. *J. Atmos. Sci.*, **76**, 3063–3087, https://doi.org/10.1175/JAS-D-18-0368.1.

Albrecht, B. A., 1993: Effects of precipitation on the thermodynamic structure of the trade wind boundary layer. *J. Geophys. Res.*, **98**, 7327–7337, https://doi.org/10.1029/93JD00027.

Albright, A. L., S. Bony, B. Stevens, and R. Vogel, 2022: Observed subcloud layer moisture and heat budgets in the trades. *J. Atmos. Sci.*, **79**, 2363–2385, https://doi.org/10.1175/JAS-D-21-0337.1.

Anurose, T., I. Bašták Ďurán, J. Schmidli, and A. Seifert, 2020: Understanding the moisture variance in precipitating shallow cumulus convection. *J. Geophys. Res. Atmos.*, **125**, e2019JD031178, https://doi.org/10.1029/2019JD031178.

Augstein, E., H. Riehl, F. Ostapoff, and V. Wagner, 1973: Mass and energy transports in an undisturbed Atlantic trade-wind flow. *Mon. Wea. Rev.*, **101**, 101–111, https://doi.org/10.1175/1520-0493(1973)101<0101:MAETIA>2.3.CO;2.

Bellon, G., and B. Stevens, 2012: Using the sensitivity of large-eddy simulations to evaluate atmospheric boundary layer models. *J. Atmos. Sci.*, **69**, 1582–1601, https://doi.org/10.1175/JAS-D-11-0160.1.

Betts, A. K., 1973: Non-precipitating cumulus convection and its parameterization. *Quart. J. Roy. Meteor. Soc.*, **99**, 178–196, https://doi.org/10.1002/qj.49709941915.

——, 1975: Parametric interpretation of trade-wind cumulus budget studies. *J. Atmos. Sci.*, **32**, 1934–1945, https://doi.org/10.1175/1520-0469(1975)032<1934:PIOTWC>2.0.CO;2.

Beucler, T., T. Cronin, and K. Emanuel, 2018: A linear response framework for radiative-convective instability. *J. Adv. Model. Earth Syst.*, **10**, 1924–1951, https://doi.org/10.1029/2018MS001280.

Blossey, P. N., and Coauthors, 2013: Marine low cloud sensitivity to an idealized climate change: The CGILS LES intercomparison. *J. Adv. Model. Earth Syst.*, **5**, 234–258, https://doi.org/10.1002/jame.20025.

Bony, S., and B. Stevens, 2019: Measuring area-averaged vertical motions with dropsondes. *J. Atmos. Sci.*, **76**, 767–783, https://doi.org/10.1175/JAS-D-18-0141.1.

——, and Coauthors, 2015: Clouds, circulation and climate sensitivity. *Nat. Geosci.*, **8**, 261–268, https://doi.org/10.1038/ngeo2398.

——, and Coauthors, 2017: EUREC^{4}A: A field campaign to elucidate the couplings between clouds, convection and circulation. *Surv. Geophys.*, **38**, 1529–1568, https://doi.org/10.1007/s10712-017-9428-0.

——, H. Schulz, J. Vial, and B. Stevens, 2020: Sugar, gravel, fish, and flowers: Dependence of mesoscale patterns of trade-wind clouds on environmental conditions. *Geophys. Res. Lett.*, **47**, e2019GL085988, https://doi.org/10.1029/2019GL085988.

Bretherton, C. S., and P. N. Blossey, 2017: Understanding mesoscale aggregation of shallow cumulus convection using large-eddy simulation. *J. Adv. Model. Earth Syst.*, **9**, 2798–2821, https://doi.org/10.1002/2017MS000981.

Cesana, G. V., and A. D. Del Genio, 2021: Observational constraint on cloud feedbacks suggests moderate climate sensitivity. *Nat. Climate Change*, **11**, 213–218, https://doi.org/10.1038/s41558-020-00970-y.

Charney, J. G., and A. Eliassen, 1964: On the growth of the hurricane depression. *J. Atmos. Sci.*, **21**, 68–75, https://doi.org/10.1175/1520-0469(1964)021<0068:OTGOTH>2.0.CO;2.

Chikira, M., 2014: Eastward-propagating intraseasonal oscillation represented by Chikira–Sugiyama cumulus parameterization. Part II: Understanding moisture variation under weak temperature gradient balance. *J. Atmos. Sci.*, **71**, 615–639, https://doi.org/10.1175/JAS-D-13-038.1.

de Roode, S. R., and A. Los, 2008: The effect of temperature and humidity fluctuations on the liquid water path of non-precipitating closed-cell stratocumulus clouds. *Quart. J. Roy. Meteor. Soc.*, **134**, 403–416, https://doi.org/10.1002/qj.222.

——, P. G. Duynkerke, and H. J. J. Jonker, 2004: Large-eddy simulation: How large is large enough? *J. Atmos. Sci.*, **61**, 403–421, https://doi.org/10.1175/1520-0469(2004)061<0403:LSHLIL>2.0.CO;2.

Denby, L., 2020: Discovering the importance of mesoscale cloud organization through unsupervised classification. *Geophys. Res. Lett.*, **47**, e2019GL085190, https://doi.org/10.1029/2019GL085190.

Emanuel, K., A. A. Wing, and E. M. Vincent, 2014: Radiative-convective instability. *J. Adv. Model. Earth Syst.*, **6**, 75–90, https://doi.org/10.1002/2013MS000270.

Fiedler, B. H., 1985: Mesoscale cellular convection: Is it convection? *Tellus*, **37A**, 163–175, https://doi.org/10.3402/tellusa.v37i2.11663.

George, G., B. Stevens, S. Bony, M. Klingebiel, and R. Vogel, 2021: Observed impact of mesoscale vertical motion on cloudiness. *J. Atmos. Sci.*, **78**, 2413–2427, https://doi.org/10.1175/JAS-D-20-0335.1.

——, ——, ——, R. Vogel, and A. K. Naumann, 2022: Ubiquity of shallow mesoscale circulations in the trades and their influence on moisture variance. *ESS Open Arch.*, https://doi.org/10.1002/essoar.10512427.1.

Grenier, H., and C. S. Bretherton, 2001: A moist PBL parameterization for large-scale models and its application to subtropical cloud-topped marine boundary layers. *Mon. Wea. Rev.*, **129**, 357–377, https://doi.org/10.1175/1520-0493(2001)129<0357:AMPPFL>2.0.CO;2.

Heinze, R., D. Mironov, and S. Raasch, 2015: Second-moment budgets in cloud topped boundary layers: A large-eddy simulation study. *J. Adv. Model. Earth Syst.*, **7**, 510–536, https://doi.org/10.1002/2014MS000376.

Held, I. M., and B. J. Hoskins, 1985: Large-scale eddies and the general circulation of the troposphere. *Adv. Geophys.*, **28**, 3–31, https://doi.org/10.1016/S0065-2687(08)60218-6.

Heus, T., and Coauthors, 2010: Formulation of and numerical studies with the Dutch Atmospheric Large-Eddy Simulation (DALES). *Geosci. Model Dev.*, **3**, 415–444, https://doi.org/10.5194/gmd-3-415-2010.

Holland, J. Z., and E. M. Rasmusson, 1973: Measurements of the atmospheric mass, energy, and momentum budgets over a 500-kilometer square of tropical ocean. *Mon. Wea. Rev.*, **101**, 44–55, https://doi.org/10.1175/1520-0493(1973)101<0044:MOTAME>2.3.CO;2.

Janssens, M., J. Vilà-Guerau de Arellano, M. Scheffer, C. Antonissen, A. P. Siebesma, and F. Glassmeier, 2021: Cloud patterns in the trades have four interpretable dimensions. *Geophys. Res. Lett.*, **48**, e2020GL091001, https://doi.org/10.1029/2020GL091001.

——, ——, C. C. van Heerwaarden, B. J. H. van Stratum, S. R. de Roode, A. P. Siebesma, and F. Glassmeier, 2023: The time scale of shallow convective self-aggregation in large-eddy simulations is sensitive to numerics. *J. Adv. Model. Earth Syst.*, **15**, e2022MS003292, https://doi.org/10.1029/2022MS003292.

Jonker, H. J., P. G. Duynkerke, and J. W. M. Cuijpers, 1999: Mesoscale fluctuations in scalars generated by boundary layer convection. *J. Atmos. Sci.*, **56**, 801–808, https://doi.org/10.1175/1520-0469(1999)056<0801:MFISGB>2.0.CO;2.

Klein, R., 2010: Scale-dependent models for atmospheric flows. *Annu. Rev. Fluid Mech.*, **42**, 249–274, https://doi.org/10.1146/annurev-fluid-121108-145537.

Klinger, C., B. Mayer, F. Jakub, T. Zinner, S.-B. Park, and P. Gentine, 2017: Effects of 3-D thermal radiation on the development of a shallow cumulus cloud field. *Atmos. Chem. Phys.*, **17**, 5477–5500, https://doi.org/10.5194/acp-17-5477-2017.

Lilly, D. K., 1996: A comparison of incompressible, anelastic and Boussinesq dynamics. *Atmos. Res.*, **40**, 143–151, https://doi.org/10.1016/0169-8095(95)00031-3.

Matheou, G., and O. Lamaakel, 2021: Growth rates of turbulence length scales in precipitating shallow cumulus convection. *2021 Fall Meeting*, New Orleans, LA, Amer. Geophys. Union, Abstract A24F-06, https://agu.confex.com/agu/fm21/meetingapp.cgi/Paper/976409.

Muller, C. J., and I. M. Held, 2012: Detailed investigation of the self-aggregation of convection in cloud-resolving simulations. *J. Atmos. Sci.*, **69**, 2551–2565, https://doi.org/10.1175/JAS-D-11-0257.1.

Müller, G., and A. Chlond, 1996: Three-dimensional numerical study of cell broadening during cold-air outbreaks. *Bound.-Layer Meteor.*, **81**, 289–323, https://doi.org/10.1007/BF02430333.

Myers, T. A., R. C. Scott, M. D. Zelinka, S. A. Klein, J. R. Norris, and P. M. Caldwell, 2021: Observational constraints on low cloud feedback reduce uncertainty of climate sensitivity. *Nat. Climate Change*, **11**, 501–507, https://doi.org/10.1038/s41558-021-01039-0.

Narenpitak, P., J. Kazil, T. Yamaguchi, P. K. Quinn, and G. Feingold, 2021: From sugar to flowers: A transition of shallow cumulus organization during ATOMIC. *J. Adv. Model. Earth Syst.*, **13**, e2021MS002619, https://doi.org/10.1029/2021MS002619.

Naumann, A. K., B. Stevens, and C. Hohenegger, 2019: A moist conceptual model for the boundary layer structure and radiatively driven shallow circulations in the trades. *J. Atmos. Sci.*, **76**, 1289–1306, https://doi.org/10.1175/JAS-D-18-0226.1.

Neelin, J. D., and I. M. Held, 1987: Modeling tropical convergence based on the moist static energy budget. *Mon. Wea. Rev.*, **115**, 3–12, https://doi.org/10.1175/1520-0493(1987)115<0003:MTCBOT>2.0.CO;2.

Nitta, T., and S. Esbensen, 1974: Heat and moisture budget analyses using BOMEX data. *Mon. Wea. Rev.*, **102**, 17–28, https://doi.org/10.1175/1520-0493(1974)102<0017:HAMBAU>2.0.CO;2.

Ouwersloot, H. G., A. F. Moene, J. J. Attema, and J. V.-G. De Arellano, 2017: Large-eddy simulation comparison of neutral flow over a canopy: Sensitivities to physical and numerical conditions, and similarity to other representations. *Bound.-Layer Meteor.*, **162**, 71–89, https://doi.org/10.1007/s10546-016-0182-5.

Park, K.-A., P. Cornillon, and D. L. Codiga, 2006: Modification of surface winds near ocean fronts: Effects of Gulf Stream rings on scatterometer (QuikSCAT, NSCAT) wind observations. *J. Geophys. Res.*, **111**, C03021, https://doi.org/10.1029/2005JC003016.

Raymond, D. J., S. L. Sessions, A. H. Sobel, and Ž. Fuchs, 2009: The mechanics of gross moist stability. *J. Adv. Model. Earth Syst.*, **1** (3), https://doi.org/10.3894/JAMES.2009.1.9.

Riehl, H., T. C. Yeh, J. S. Malkus, and N. E. La Seur, 1951: The north-east trade of the Pacific Ocean. *Quart. J. Roy. Meteor. Soc.*, **77**, 598–626, https://doi.org/10.1002/qj.49707733405.

Schulz, H., R. Eastman, and B. Stevens, 2021: Characterization and evolution of organized shallow convection in the downstream North Atlantic trades. *J. Geophys. Res. Atmos.*, **126**, e2021JD034575, https://doi.org/10.1029/2021JD034575.

Seifert, A., and T. Heus, 2013: Large-eddy simulation of organized precipitating trade wind cumulus clouds. *Atmos. Chem. Phys.*, **13**, 5631–5645, https://doi.org/10.5194/acp-13-5631-2013.

——, ——, R. Pincus, and B. Stevens, 2015: Large-eddy simulation of the transient and near-equilibrium behavior of precipitating shallow convection. *J. Adv. Model. Earth Syst.*, **7**, 1918–1937, https://doi.org/10.1002/2015MS000489.

Siebesma, A. P., and J. W. M. Cuijpers, 1995: Evaluation of parametric assumptions for shallow cumulus convection. *J. Atmos. Sci.*, **52**, 650–666, https://doi.org/10.1175/1520-0469(1995)052<0650:EOPAFS>2.0.CO;2.

——, and Coauthors, 2003: A large eddy simulation intercomparison study of shallow cumulus convection. *J. Atmos. Sci.*, **60**, 1201–1219, https://doi.org/10.1175/1520-0469(2003)60<1201:ALESIS>2.0.CO;2.

Sobel, A. H., J. Nilsson, and L. M. Polvani, 2001: The weak temperature gradient approximation and balanced tropical moisture waves. *J. Atmos. Sci.*, **58**, 3650–3665, https://doi.org/10.1175/1520-0469(2001)058<3650:TWTGAA>2.0.CO;2.

Stevens, B., 2007: On the growth of layers of nonprecipitating cumulus convection. *J. Atmos. Sci.*, **64**, 2916–2931, https://doi.org/10.1175/JAS3983.1.

——, and Coauthors, 2020: Sugar, gravel, fish and flowers: Mesoscale cloud patterns in the trade winds. *Quart. J. Roy. Meteor. Soc.*, **146**, 141–152, https://doi.org/10.1002/qj.3662.

——, and Coauthors, 2021: EUREC^{4}A. *Earth Syst. Sci. Data*, **13**, 4067–4119, https://doi.org/10.5194/essd-13-4067-2021.

Thomas, M. L., I. Bašták Ďurán, and J. Schmidli, 2021: Toward parametrization of precipitating shallow cumulus cloud organization via moisture variance. *J. Geophys. Res. Atmos.*, **126**, e2021JD034939, https://doi.org/10.1029/2021JD034939.

Tobin, I., S. Bony, and R. Roca, 2012: Observational evidence for relationships between the degree of aggregation of deep convection, water vapor, surface fluxes, and radiation. *J. Climate*, **25**, 6885–6904, https://doi.org/10.1175/JCLI-D-11-00258.1.

van Zanten, M. C., and Coauthors, 2011: Controls on precipitation and cloudiness in simulations of trade-wind cumulus as observed during RICO. *J. Adv. Model. Earth Syst.*, **3**, M06001, https://doi.org/10.1029/2011MS000056.

Vogel, R., L. Nuijens, and B. Stevens, 2016: The role of precipitation and spatial organization in the response of trade-wind clouds to warming. *J. Adv. Model. Earth Syst.*, **8**, 843–862, https://doi.org/10.1002/2015MS000568.

——, S. Bony, and B. Stevens, 2020a: Estimating the shallow convective mass flux from the subcloud-layer mass budget. *J. Atmos. Sci.*, **77**, 1559–1574, https://doi.org/10.1175/JAS-D-19-0135.1.

——, L. Nuijens, and B. Stevens, 2020b: Influence of deepening and mesoscale organization of shallow convection on stratiform

cloudiness in the downstream trades. *Quart. J. Roy. Meteor. Soc.*, **146**, 174–185, https://doi.org/10.1002/qj.3664.

Wing, A. A., and Coauthors, 2020: Clouds and convective self-aggregation in a multimodel ensemble of radiative-convective equilibrium simulations. *J. Adv. Model. Earth Syst.*, **12**, e2020MS002138, https://doi.org/10.1029/2020MS002138.

Wood, R., and D. L. Hartmann, 2006: Spatial variability of liquid water path in marine low cloud: The importance of mesoscale cellular convection. *J. Climate*, **19**, 1748–1764, https://doi.org/10.1175/JCLI3702.1.

Yanai, M., S. Esbensen, and J.-H. Chu, 1973: Determination of bulk properties of tropical cloud clusters from large-scale heat and moisture budgets. *J. Atmos. Sci.*, **30**, 611–627, https://doi.org/10.1175/1520-0469(1973)030<0611:DOBPOT>2.0.CO;2.

Zelinka, M. D., T. A. Myers, D. T. McCoy, S. Po-Chedley, P. M. Caldwell, P. Ceppi, S. A. Klein, and K. E. Taylor, 2020: Causes of higher climate sensitivity in CMIP6 models. *Geophys. Res. Lett.*, **47**, e2019GL085782, https://doi.org/10.1029/2019GL085782.

Zuidema, P., G. Torri, C. Muller, and A. Chandra, 2017: A survey of precipitation-induced atmospheric cold pools over oceans and their interactions with the larger-scale environment. *Surv. Geophys.*, **38**, 1283–1305, https://doi.org/10.1007/s10712-017-9447-x.